ALMA Mapping of Molecular Gas and Dust in the Post-AGB Star IRAS 15445-5449.

Marcela Echeverri Gallego

Trabajo de grado para optar al título de Astrónoma

Asesor
Andrés Pérez Sánchez, PhD
Esteban Silva Villa, PhD

Universidad de Antioquia
Facultad de Ciencias Exactas y Naturales
Instituto de Física
Medellín
2025

Universidad de Antioquia
Instituto de Física
Facultad de Ciencias Exactas y Naturales

ALMA Mapping of Molecular Gas and Dust in the Post-AGB Star IRAS 15445-5449.

Undergraduate Thesis

MARCELA ECHEVERRI GALLEGO

Advisor: Andrés Pérez Sánchez
Co-advisor: Esteban Silva Villa

Medellín, 2025

Universidad de Antioquia

Universidad de Antioquia
Instituto de Física
Facultad de Ciencias Exactas y Naturales

ALMA Mapping of Molecular Gas and Dust in the Post-AGB Star IRAS 15445-5449.

Undergraduate Thesis

MARCELA ECHEVERRI GALLEGO

Advisor: Andrés Pérez Sánchez
Co-advisor: Esteban Silva Villa

Medellín, 2025

Abstract

Stars with masses below $9, M_{\odot}$ eject most of their stellar envelopes during their evolution along the Asymptotic Giant Branch (AGB). The resulting circumstellar regions provide density and temperature conditions that favor the formation of dust and molecular gas. In post-AGB stars, molecules such as H_2O, ^{12}CO, ^{13}CO, SO_2, and OH have been detected, but the spatial and kinematic distribution of the material in their envelopes remains poorly understood. In this work, we focus on the circumstellar envelope of the post-AGB star IRAS 15445-5449. Using ALMA submillimeter observations, we analyzed molecular emission lines of ^{13}CO and SO_2, as well as the dust continuum. We processed the data with the Common Astronomy Software Applications (CASA) to generate moment maps and position–velocity diagrams.

Our results reveal an oxygen-rich environment with high-velocity shocks (> 40 km/s), consistent with J-shock conditions. The emission traces a collimated bipolar morphology, indicating that the gas dynamics are dominated by expansion rather than rotation. We find spatial overlap between dust and molecular gas, suggesting active post-shock reformation. Based on the ^{13}CO (J = 3 – 2) line, we redefine the systemic velocity of the source to $v_{sys} = -85.8$ km/s. We also recover the sizes of key structures, including the base of the bipolar outflow and the region traced by low-velocity gas.

Keywords

Post-AGB Stars, Circumstellar Envelopes, ALMA Observations, Molecular Line Emission, Shock Chemistry, Dust Continuum, Moment Maps

No hay espectáculo más hermoso que el cielo estrellado, porque nos recuerda nuestra pequeñez y nuestra capacidad de asombro.

Contents

Chapter 1

Introduction

1.1 Stellar Evolution Beyond the Main Sequence

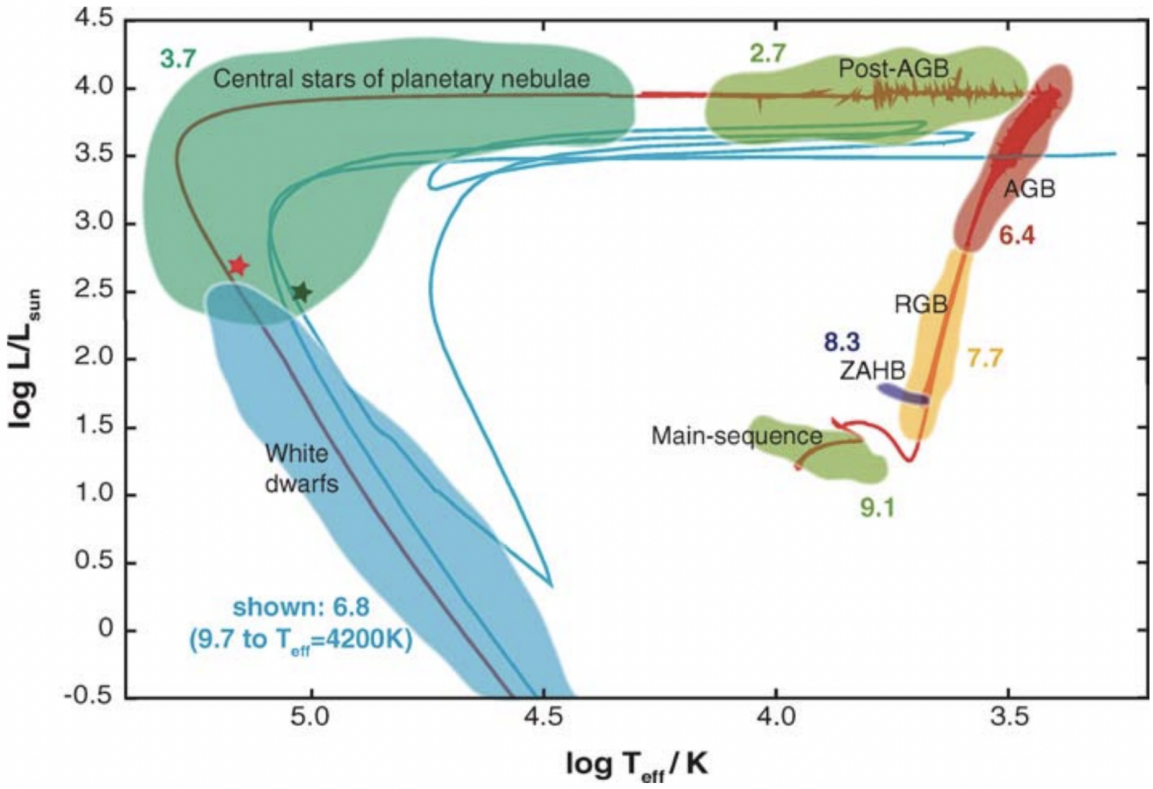

Figure 1.1: *Synthetic evolutionary track for a 2 $M_\odot$ star of solar metallicity on the Hertzsprung-Russell diagram. Numbers labeled on each phase represent the log of the time it takes for the star to pass through. Adopted from Herwig (2005).*

Stars are objects that humanity has studied for centuries, seeking to understand the bright points that appear at night. The evolution and classification of different stars were recently formally studied. In the early 20th century, the characteristics of main-sequence stars were defined, and shortly after, the terms "giant" and "dwarf" stars were introduced (Arp et al., 1953). Later, during the 1930s, accurate models of the structure of main-sequence stars were developed, but the fitting of red giants into stellar evolution remained poorly understood. The study of the late

stages of stellar evolution began after World War II (Habing and Olofsson, 2013). The combination of better observations of globular clusters and increased computational power for simulations and models facilitated the study of individual stars. This progress marked the beginning of the detailed study of post-main sequence stars that led to the understanding of the evolutionary track of low- and intermediate-mass stars beyond the Red Giant Branch (RGB), that is: Asymptotic Giant Branch (AGB), post-AGB, Planetary Nebulae (PNe), and White Dwarf (WD). As seen in Figure 1.1.

1.1.1 Asymptotic Giant Branch Stars

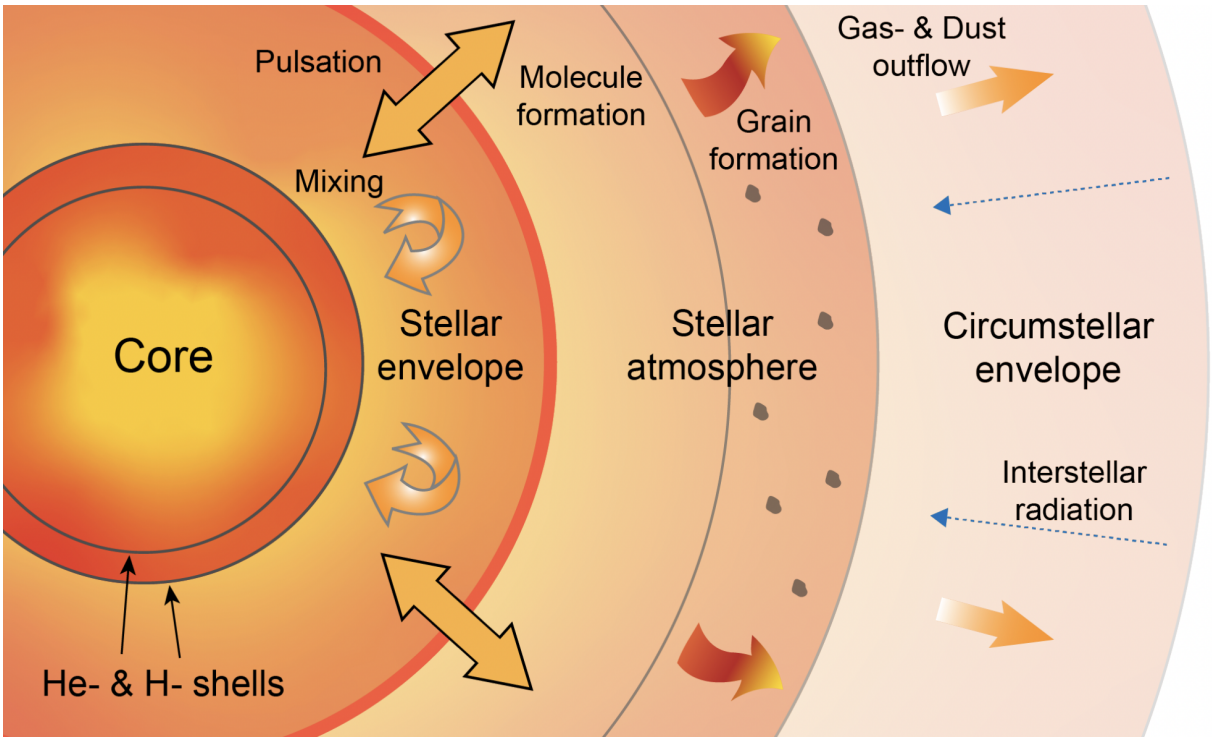

Figure 1.2: *AGB and post-AGB star structure diagram. Adopted from Alm et al. (2019) as an adaptation of the same diagram from Habing and Olofsson (2013).*

Early studies of stars in globular clusters led to an unexpected discovery on their color-magnitude diagram, described by researchers as a "bifurcation of the red giant branch" (Arp et al., 1953). The unexpected region was later identified as the AGB phase, and now, the structure of these types of stars is well understood. Figure 1.2 is a schematic view of the structure of these types of stars.

After leaving the main sequence, low- and intermediate-mass stars (less than $9M_{\odot}$) evolve along the Hertzsprung-Russell (HR) diagram through the RGB. Thus, after burning most of the Hydrogen and Helium in their core, they reach the Zero-Age Horizontal Branch (ZAHB) where core helium burning takes place, and subsequently continue their evolution along the AGB phase in a high-luminosity and low-temperature region of the Hertzsprung-Russell (HR) diagram (See

Figure 1.1). An AGB star contains a small, hot, and dense degenerate core composed primarily of carbon and oxygen, which is the remnant of previous helium-core burning. The core is surrounded by a hydrogen-burning shell and a helium-burning shell where nuclear processing occurs. Surrounding the core, there is a large, hot, but less dense stellar envelope, followed by a tenuous atmosphere (Herwig, 2005). The structure of AGB stars is made by a combination of chemical and physical processes that co-occur in different regions of the star. Among these processes, thermal pulses, nucleosynthesis, dredge-ups, and mass loss are particularly important.

As the star continues to evolve, material in the core increases because of nucleosynthesis, and luminosity increases gradually. The material surrounding the core is being dispersed into space, building the AGB structure. When the temperature of the star increases with a constant luminosity, the AGB phase becomes the post-AGB phase (see Figure 1.1). AGB structure becomes optically thick, and it causes the central star to not be directly observable. It is the reason why, in observational studies, it is complicated to define what objects can be classified as post-AGB stars.

There are some different criteria to classify stars as post-AGB. Habing and Olofsson (2013) defined some boundaries on the HR diagram based on the properties of the central star, to determine if a stellar object is a post-AGB or not. Their study suggests spectral types in the range of K to B with luminosity class I to III as a delimiter, including a few exceptions. Another classification criterion is the chemical composition of the photosphere. It is not expected to find post-AGB stars at a high galactic latitude, as population I stars with I to III luminosity class tend to be found close to the galactic plane. Selection criteria can be far from the star to the circumstellar environment. Cold dust, ejected by the star during the AGB phase, is shaping the first stage of the circumstellar environment. This dust is the reason why many post-AGB stars have been identified from their infrared Spectral Energy Distributions (SEDs). In the early stages of circumstellar environment expansion, the increased optical depth produces a characteristic double-peaked shape in the SED (Habing and Olofsson, 2013). AGB stars can also satisfy some of these criteria, so it is difficult to differentiate between late AGB and early post-AGB stars. The post-AGB phase begins when the strong pulsations and heavy mass loss of the AGB cease. O-rich post-AGB stars are distinguishable from AGB stars by their lack of variation in IR luminosity and OH maser line strength.

1.1.2 Circumestrellar Envelopes

Due to thermal pulses and other mechanisms, AGB stars begin to lose mass through a slow wind. At the beginning, mass loss rate is on the order of $\dot{M} = 1 \times 10^{-8} M_{\odot}$ yr^{-1} but it increases over time until the end of AGB phase, where it can have values up to $\dot{M} = 1 \times 10^{-4} M_{\odot}$ yr^{-1} (Habing and Olofsson, 2013). Velocity of this wind is $\sim$ 5–15 km/s, which is slow compared to the solar wind of $\sim$ 500 km/s, even if Sun's mass-loss rate is lower $1 \times 10^{-14} M_{\odot}$ yr^{-1} (Pérez-Sánchez et al., 2011). As illustrated in Figure 1.2, at a certain distance from the star (approximately 5 $R_{\star}$), temperature and density conditions lead to dust formation (Habing and Olofsson, 2013). The numbers shown in Figure 1.1 correspond to the logarithm of the time the star remains in each

phase. According to the numerical model by (Herwig, 2005), the evolution of a $2M_{\odot}$ mass star lasts a few thousand years ($\sim 10^3$ yr). In this case, time is inversely proportional to initial mass; for smaller or higher initial masses, the duration of the phase is going to be higher or smaller, respectively. That is the reason why post-AGB stars are difficult to find; this stage of stellar evolution lasts for a short time compared to other phases.

A common characteristic of post-AGB stars is the presence of an extended Circumstellar Envelope (CSE). Due to their physical properties, CSEs have density and temperature conditions that favor the formation of dust and molecular gas (Habing and Olofsson, 2013). Molecules such as water (H_2O), carbon monoxide and its isotopes (CO, ^{12}CO, ^{13}CO, ...), sulfur dioxide (SO_2), hydroxyl (OH), silicon monoxide (SiO), among others, have been detected in the CSEs of post-AGB objects (Pérez Sánchez, 2014; Contreras et al., 2018). For this type of star, the spatial and kinematic distribution of its material remains poorly understood. The formation and distribution of molecules depend on factors such as their UV tolerance, formation mechanisms, as well as the interactions with other molecules in the medium. Each molecule may be distributed at different radii from the central star, which plays a key role in shaping the CSE. Additionally, the conditions in these envelopes are favorable for the accretion of solid material and the formation of dust particles, but in regions farther away from the central star.

The material in the CSEs of AGB stars can be oxygen-rich or carbon-rich, depending on the evolution process of the star. The molecular composition and chemistry of a CSE are determined by this factor. Studying molecules in CSEs provides valuable information about the central star, such as its main-sequence mass, mass-loss rate, and initial composition (Alm et al., 2019). Additionally, the morphology of a CSE can offer clues about the future formation of a Planetary Nebula (PN). During the post-AGB phase, CSEs continue to expand and cool, gradually revealing the central star (Herwig, 2005). Eventually, the star becomes a white dwarf, and the remaining CSE material forms a PN.

1.1.3 Planetary Nebulae Morphology

Planetary Nebulae (PNe) are outstanding stellar objects composed of a stellar core, normally called White Dwarf (WD), surrounded by an extended distribution of ionized gas. PNe are also the remnant material of a star at the end of its stellar evolution process. Historically, we discovered them before Red Giants (RG) and WD stars, which makes sense because they are larger, easier to observe, and more visually interesting than a single star (Habing and Olofsson, 2013). Curiously, an open problem in astronomy is the wide variety of morphologies of PNe. In general and for simplicity of the numerical models, the mass-loss process of an AGB/post-AGB star is assumed to be spherically symmetric, resulting in PNe with idealized spherical shapes. However, from observations we can infer that this is not the case. The physical processes involved in the formation of complex shapes in PNe remain unknown, as a high percentage of them exhibit asymmetries, elliptical shapes, or multi-polar distributions. See Figure 1.3 for reference on what these type of objects looks like.

The study of post-AGB sources and their mass-loss process is key to understanding the morphology of PNe. It has been observed that some post-AGB stars have axisymmetric outflows, and a synchrotron jet has been found in one of these sources (Pérez-Sánchez et al., 2013). Although the central star has fast stellar winds, radiation pressure does not have enough energy to move the large amounts of material observed by itself. The mechanism that could eject all material exclusively in an axial direction remains unknown. It could be driven by the interaction with a stellar or sub-stellar companion or a large-scale magnetic field, but this is still under debate (Pérez Sánchez, 2014).

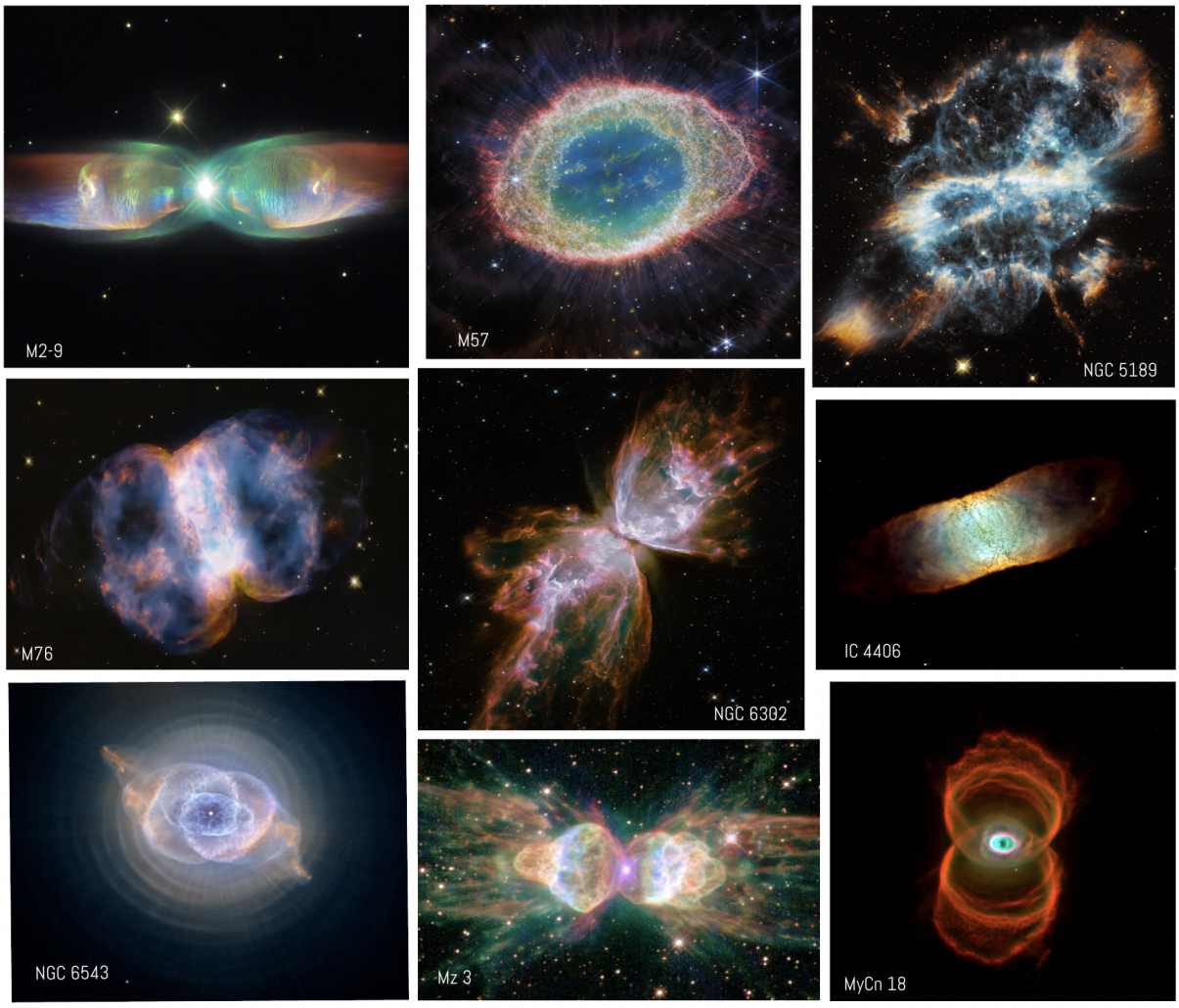

Figure 1.3: *Variety of Planetary Nebulae morphologies. Credits: Hubble Legacy Archive, ESA/Webb, NASA.*

High-velocity outflows from post-AGB stars generate shock regions that create conditions favorable for the formation of molecules. The detection of specific molecules (known as shock tracers) in the CSE of a post-AGB star indicates the presence of a shock region, where particles are moving at high velocities. Shocked regions are not exclusive to the final phases of stellar evolution. Shocks are studied in many types of astronomical sources and phenomena, like Supernova remnants, Young stellar objects, Active Galactic Nuclei, and ISM Bow shocks, among others.

Molecular shocks are a key mechanism for the formation and destruction of complex molecules, helping to enrich the interstellar medium.

1.2 Fast Interstellar Shocks in Molecular Clouds

Shocks are a common natural phenomenon; almost every disturbance in a medium can generate a shock wave. The interstellar medium is not the exception; gas and dust clouds are often disrupted by events such as supernova explosions, stellar winds, and cloud-cloud collisions (Hollenbach and McKee, 1989). A shock wave is a pressure-driven disturbance and represents an irreversible process, converting ordered kinetic energy into disordered thermal energy (Draine and McKee, 1993). As the shock wave propagates through the medium, the post-shock region undergoes changes in temperature, pressure, chemical composition, and its kinetic field.

1.2.1 Shocks in dense regions

Shocks are classified based on their impact on the medium, commonly as C-shocks or J-shocks. This classification depends on propagation velocity, environmental ionization, and magnetic field intensity (Draine and McKee, 1993). In C-shocks, gas is accelerated and heated through particle collisions between neutral gas (with temperatures not exceeding 3000 – 4000 K) and charged particles. C-shocks occur in weakly ionized molecular gas with velocities below 40 – 50 km/s (Hollenbach and McKee, 1989). As changes in the physical conditions of the medium are gradual, C shocks are known as Continuous shocks.

On the other hand, J-shocks are high-velocity shocks occurring in atomic or ionized gas, or molecular clouds at velocities greater than 40–50 km/s (Hollenbach and McKee, 1989). Known as Jump shocks, they take their name from the sudden changes in parameters such as temperature, density, and pressure due to the fast propagation of the shock wave. J-shocks emit UV radiation capable of pre-ionizing or pre-dissociating gas in molecular clouds, a critical process for forming complex molecules (Draine and McKee, 1993). The evolution of the circumstellar envelope of an AGB or post-AGB star is closely linked to shock processes (Habing and Olofsson, 2013). Regions with fast interstellar shocks are typically rich in molecules, with dust playing a crucial role in molecular formation processes.

1.2.2 Molecule and Dust Grain Formation in Dense Clouds

Observations of CSEs in post-AGB stars reveal the presence of molecules that could not exist without post-shock regions (Contreras et al., 2018). Fast shocks, particularly J-shocks, alter the conditions of interstellar clouds, creating an ideal environment for molecules and dust grains to interact and form complex molecules. This process enriches the CSE, and the resulting molecular composition will depend on the available material and elemental abundances. These conditions lead to a number of important chemical processes with the rest of the material in the envelope. Some of them include collisional dissociation and ionization, photo-dissociation by UV radiation produced in the hot shock front, neutral-neutral reactions, and the reformation of H_2 on warm

gas regions on the surface of dust grains (Hollenbach et al., 2013).

First, pre-shock gas is disturbed by the approaching shock, experiencing a radiation field. J-shocks on a molecular cloud first dissociate the molecules and partially destroy dust grains due to the high temperatures and UV radiation after the passing of the shock front. Then, the temperature of the post-shock region is determined by the balance between heating and cooling. In this process, the principal cooling mechanisms are the Lyman-alpha emission, emission from the cold dust grains, H_2 dissociation, CO rotational and vibrational emission, and H_2O rotational emission. On the other hand, the principal heating mechanisms are photo-ionization, pumping of the Lyman and Werner bands of H_2 by Lyα photons, and H_2 formation on grain surfaces. The efficiency of all of these mechanisms to cool or heat the gas depends on the temperature distribution and column density of the post-shock region (Neufeld and Hollenbach, 1994).

During the cooling, the post-shock region goes through changes in temperature and density. Right after the shock, the gas temperature reaches values of 1×10^4 K, as is shown in Hollenbach and McKee (1989) models. The molecular hydrogen that was dissociated starts to reform on the surface of the surviving dust grains with a certain effective recombination rate (Hollenbach and McKee, 1989). Here initiates the production of all other molecules. H_2 molecules start to be ejected from dust grains into the gas phase with an internal energy that heats the medium (only if post-shock density is $\geq 1 \times 10^6$ cm^{-3}, Hollenbach et al., 2013) and balances with cooling mechanisms. The heating produces good conditions to form molecules in something called "H_2 reformation plateau" that has a temperature of $100 - 400$ K. This plateau is nearly isothermal and isochoric, but also, if the cloud is O-rich, it is warm enough to form specifically oxygen-bearing molecules as OH, H_2O, among others (Hollenbach and McKee, 1989). Chemical reactions require different activation energies depending on the type of molecule that is formed.

The oxygen chemistry in shocked molecular gas regions described in Hollenbach and McKee (1989) starts with the reaction,

$$H_2 + O \rightarrow OH + H$$

This causes a series of neutral-neutral reactions on the plateau. Rapidly, CO forms due to the interaction of C and C^+ with the resultant OH as follows:

$$C + OH \rightarrow CO + H$$

As CO has three times the binding energy of H_2, when almost every carbon is locked with the available oxygen, the remaining oxygen that formed OH and the reformed H_2 that is also available, forms H_2O. That's why water abundance in these types of regions depends on the abundance of oxygen in the pre-shock region. The reaction that leads to the formation of water is:

$$OH + H_2 \rightarrow H_2O + H$$

These three molecules, OH, CO, and H_2O, are key coolants of the gas. While the previously

described reactions represent the main formation pathways, numerous secondary reactions can also contribute to their production (Hollenbach and McKee, 1989). Finally, once H_2 reformation is complete, almost all the oxygen is locked in H_2O.

All of this process depends on different parameters that lead to the final results of abundances and physics in the post-shock region. There are a lot of computational models that study the post-shock region from pre-shock parameters and the velocity of the shock (e.g. Hollenbach and McKee, 1989; Neufeld and Hollenbach, 1994; Hollenbach et al., 2013; Hartigan et al., 1987; Neufeld, 1987; Guillet et al., 2009; Flower and Pineau Des Forêts, 2010). The models show that if the velocity is too low (< 15 km/s), the gas is too cold to reach molecule formation. If the velocity is too high (> 100 km/s), all the dust grains will be sublimated. As we said before, dust grains are fundamental in the reformation of H_2; without them, it would be difficult for molecules to form. It is the same with pre-shock density; some boundaries determine the formation of molecules, specifically for water masers. At high pre-shock densities (10^7 cm^{-3} $< n_0 <$ 10^9 cm^{-3}) and low velocities (15 km/s $< v <$ 40 km/s), some C-shocks can form water, but at lower pre-shock densities with the same velocity range, there is not sufficient energy to reach the temperature of the re-formation plateau. For high velocities (40 km/s $< v <$ 160 km/s), pre-shock density ranges could be higher (10^5 cm^{-3} $< n_0 <$ 10^8 cm^{-3}) and with these conditions, J-shocks can form water.

1.3 Radiative Transfer

Light is essential to human life. For astronomers, as we can't experiment with stars, planets, or galaxies, light is the only way that we have for studying astronomical objects. Light is electromagnetic radiation propagating through space with different levels of energy. As Newton did with prisms in 1672, we can decompose light into a spectrum depending on its energy value (Rybicki and Lightman, 2004). The electromagnetic spectrum ranges from high-energy radiation such as gamma rays to low-energy radiation such as radio waves. In astronomy, we observe different properties of sources depending on the measured radiation. On its way through space, light interacts with all kinds of objects, losing or gaining energy by emission or absorption of photons.

The specific intensity along the path that radiation follows depends on the emission (j_ν) and absorption (α_ν) coefficients. These coefficients describe the effects of matter interacting with light (note that both depend on the frequency ν). The rate between emission and absorption is called the source function ($S_\nu = j_\nu/\alpha_\nu$) and is normally a simpler way to describe the physical process (Rybicki and Lightman, 2004). In 1916, Einstein introduced three fundamental processes that describe the probability of absorption and emission of photons, quantified by the so-called Einstein coefficients (Einstein, 1916):

- **Spontaneous emission**, where a system goes from a high energy level to a low energy level by emitting a photon, occurring without the need for an external radiation field.
- **Absorption**, a transition from a lower to a higher energy level because of the presence of a radiation field.

- **Stimulated Emission**, where an electron in a system goes from a high energy level to a low energy level due to the interaction with a photon of a specific frequency.

Later, in 1927, Paul Dirac derived expressions for Einstein's coefficients describing the quantum theory of the emission and absorption of radiation (Dirac, 1927). The coefficients j_ν and α_ν could be estimated for upper (u) and lower (l) energy states of a particular transition (Rybicki and Lightman, 2004).

$$j_\nu = \frac{h\nu_{ul}}{4\pi} A_{ul} \phi_{u,\nu} N_u \tag{1.1}$$

$$\alpha_\nu = \frac{h\nu_{ul}}{4\pi} (N_l B_{lu} \phi_{l,\nu} - N_u B_{ul} \phi_{u,\nu}) \tag{1.2}$$

where N_u and N_l are the number density of molecules at upper and lower levels, respectively, and $\phi_{i,\nu}$ is the line profile given by the velocity distribution for every energy state. For radio frequencies, it is possible to use an approximation where $\phi_{l,\nu} = \phi_{u,\nu} = \phi_\nu$. In this case, an explicit form of the source function could be estimated using Equation 1.1 and 1.2.

$$S_\nu = \frac{A_{ul} N_u}{N_l B_{lu} - N_u B_{ul}} \tag{1.3}$$

A_{ul}, B_{lu} and B_{lu} are the Einstein coefficients that satisfy the relations $A_{ul}/B_{ul} = 2h\nu_{ul}^3/c^2$ and $B_{lu}/B_{ul} = g_u/g_l$. g_i is the statistical weight of energy levels and could be used to calculate the number density per sub-level $n_i = N_i/g_i$. From these relations, the source function becomes

$$S_\nu = \frac{2h\nu_{ul}^3}{c^2} \left(\frac{n_l}{n_u} - 1 \right)^{-1} \tag{1.4}$$

To obtain the emitting intensity along a path in a medium, it is possible to incorporate the emission and absorption effects on a single equation called the radiative transfer equation (Rybicki and Lightman, 2004).

$$\frac{dI_\nu}{ds} = -\alpha_\nu I_\nu + j_\nu \tag{1.5}$$

As intensity depends on the frequency, we can define the optical depth ($\tau_\nu = \alpha_\nu ds$) as a measure of the transparency of the medium due to absorption. Using this relation in Equation 1.5, we can obtain the radiative transfer equation in terms of source function and optical depth.

$$\frac{dI_\nu}{d\tau_\nu} = -I_\nu + S_\nu \tag{1.6}$$

When $\tau_\nu > 1$, the medium is opaque or optically thick, but when $\tau_\nu < 1$, the medium is transparent or optically thin (Carroll and Ostlie, 2017). Similarly, the average distance a photon can travel through a medium without being absorbed is called the mean free path (l_ν), and for homogeneous materials, it is inversely proportional to the absorption coefficient ($l_\nu = 1/\alpha_\nu$). As the optical depth depends on the frequency (or wavelength), a medium could be transparent and opaque at the same time in different parts of the spectrum. For example, the Earth's atmosphere is optically thin at visible wavelengths but is optically thick at X-ray wavelengths (Carroll and Ostlie, 2017). Specifically for molecular gas in CSEs of AGB or post-AGB stars, the solution of

the radiative transfer equation and the form of the source function could be calculated knowing the distribution of the level population of the molecular species present in the CSEs. There are models for that type of calculation focused on specific sources and molecules (Pérez Sánchez, 2014).

1.4 Interferometry Concepts

For the study of CSEs, it is essential to go deeper into one part of the spectrum, the radio astronomy regime. For radio frequencies, we can detect different emission lines from objects that are too cold to produce visible light as CSEs of AGB or post-AGB stars. Radio Astronomy is a relatively new field; however, it has developed very quickly. In December of 1932, Karl Jansky made the first successful radio detection of an astronomical object, the galactic center of the Milky Way. It was the start of the development of radio astronomy in the world. Over a couple of decades, radio astronomy yielded discoveries as quasars, pulsars, and the cosmic microwave background (see Marr et al., 2015, for further reading). For 1974, half of the Nobel Prize in physics was awarded to Sir Martin Ryle for pioneering in aperture synthesis, and the other half was awarded to Antony Hewish for the discovery of pulsars with radio observations (Ryle, 1952; Hewish et al., 1979). Today, radio astronomy observations have the same impact as visible wavelength astronomy.

A single radio telescope has different parts to function properly. In general, it has a dish or reflector that collects and focuses waves, a feed that captures the concentrated radio waves and converts them into electrical signals, a transmission line that is in charge of ensuring that the weak signals remain strong enough for analysis and a receiver that amplifies and processes the signals, filtering out noise to start astronomical processing. The reflector of the telescope works as a circular aperture, and when the waves interact with the dish, it behaves as if light passes through a circular aperture and generates a diffraction pattern (Marr et al., 2015). For a single dish, the angular resolution of the observations depends inversely on the diameter of the plate (D) as $\theta = \lambda/D$. The larger the dish, the better the resolution. But imagine you need to observe at $\lambda = 10$ cm with a resolution similar to visible observations $\approx 2 \times 10^{-5}$ rad. Calculating the size of the telescope with the previous relation, $D \approx 5$ km. It is almost impossible to build an antenna of 5 km in diameter.

Motivated by the physical limitations, astronomers developed a technique called *aperture synthesis*. Using a large number of telescopes organized in an array, we can synthesize a new telescope with a very large diameter. It starts taking data at the same time with every antenna and combines the observations of every single pair of telescopes in the array using interferometry. Then, it is possible to mathematically process the data and produce the equivalent resolution of a single dish of a telescope with a diameter equal to the longest distance between a pair of antennas in the array(Marr et al., 2015). There is a simpler configuration of only two antennas separated by a distance B (called the baseline). As these two antennas are separated by a certain distance, there is a time delay on the signal received, which causes a phase difference between the two signals and has to be corrected. Once all signals have the same phase, the reconstruction process

uses constructive and destructive interference phenomena by combining the signal with Fourier transformation techniques to obtain the best image.

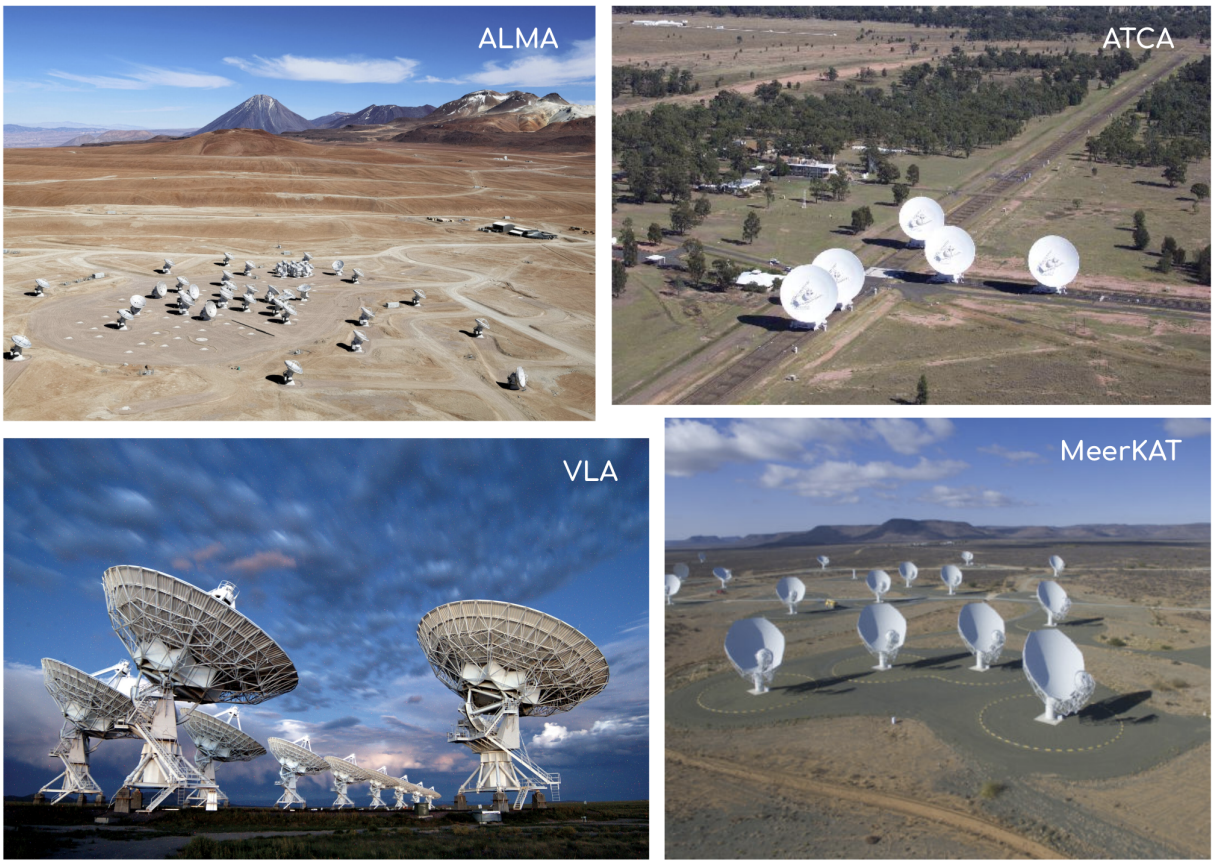

Figure 1.4: *Interferometers around the world. Upper left: ALMA (Atacama Large Millimeter/Submillimeter Array). Upper right: ATCA (Australia Telescope Compact Array). Lower left: VLA (Very Large Array). Lower right: MeerKAT (Karoo Array Telescope). Credits: NRAO/AUI/NSF, Clem and Adri Bacri-Normier, CSIRO Australia (08-Sep-2005), NRF/SARAO.*

With this technique, the resolution of the observations increases, but not the sensitivity. This parameter depends on the total collecting area; for two radio antennas, it is too low, and we lose a lot of information about the sources. So we use arrays of large numbers of antennas placed in different configurations, trying to maximize the sensitivity of the observations without losing resolution (Marr et al., 2015). This concept can be extrapolated to observations with radio telescopes all over the world, to obtain a baseline of the size of entire countries (as in the Very Large Baseline Array, VLBA, with a baseline of the size of the United States) or even the size of the Earth (as in the Event Horizon Telescope, EHT). This technique is called VLBI (Very Long Baseline Interferometry), and the data needs new corrections and calibrations due to the effects of the rotation of the Earth and the physical differences between telescopes (different antennas with different diameters and variations on the transmission lines). As this process is too complex, a more detailed description of the methods of interferometry and synthesis of radio astronomical images can be found in (Thompson et al., 2017).

Located on all continents, radio telescopes around the world can observe a large part of our sky and cover different portions of the radio spectrum. Interferometers (See Figure 1.4 for visual reference) such as VLA (Very Large Array) with 27 antennas of 25 meters, ATCA (Australia Telescope Compact Array) with 6 antennas of 22 meters, MeerKAT (Karoo Array Telescope) with 64 antennas of 13.5 meters and ALMA (Atacama Large Millimeter/Submillimeter Array) with 54 antennas of 12 meters and 12 antennas of 7 meters, among others, use aperture synthesis for taking data. ALMA is the largest radio telescope array in the world, and is located in the north of Chile at > 5100 meters above sea level. The distances between the antennas could vary between 150 meters and 16 kilometers, which makes it a very powerful tool to observe with high resolution and high sensitivity. The wavelengths (or frequencies) that ALMA can observe are special for observing cold sources in radio that cover different astronomical objects and processes as exoplanets, the formation and evolution of planetary systems, highly evolved stars, planetary nebulae, the formation of galaxies, cold objects in our solar system, and even black holes. In that sense, ALMA observations are perfect for studying molecule distributions on CSEs in AGB and post-AGB stars.

1.5 The post-AGB star: IRAS 15445-5449

The post-AGB star IRAS 15445-5449 was first detected in OH transitions at 1612 MHz, looking for sample stellar dynamics on the galactic plane, in a survey in 1994 (Sevenster et al., 1997). Then, the source was detected with another two OH transitions at 1665 MHz and 1667 MHz (Caswell, 1998). From there, new observations of 1612 MHz, 1665 MHz, and 1667 Hz were performed in 2003 (Deacon et al., 2004). They classified IRAS 15445-5449 as a post-AGB star according to its Midcourse Space Experiment (MSX) and Infrared Astronomical Satellite (IRAS) color diagrams. The 22 GHz H_2O masers were first detected in observations from 2004 and helped to classify the source as a Water Fountain (WF) in 2007 (Deacon et al., 2007). The OH profiles were extremely wide with emission velocities from -200 to -100 km/s, while H_2O profiles showed some narrow features separated from each other on a range between -145 to -54 km/s (Deacon et al., 2004). As OH lines were classified as irregular line profiles (Deacon et al., 2004, 2007), line morphology suggested that IRAS 15445-5449 could be a bipolar object with outflows and remnant AGB wind. Contrary to expectations from theory, none of the OH profiles were double-peaked. Therefore, the systemic velocity of the source was assumed to be $v_{sys} = -150$ km/s (Deacon et al., 2007).

Although the source had already been classified as a post-AGB star, in 2007 it was also included in a catalog of Young Stellar Objects (YSO) candidates (Urquhart et al., 2007b). The classification of a massive YSO was supported by a strong ^{13}CO (J = 1 - 0) emission line detected at -44 km/s (Urquhart et al., 2007a). The center velocity reported had to be the systemic velocity, which is not consistent with previous results. There is known to be significant Galactic CO emission at around -40 km/s, which could indicate that the strong ^{13}CO (J = 1 – 0) emission arises from the Galactic plane and not from the source. See Pérez-Sánchez et al. (2013) for more details.

Later, in 2009 Bains et al. (2009) reported the first radio continuum detections of all bar on IRAS 15445-5449, identifying the presence of dust shells around the central star. Bains et al. (2009) also reported a total line-of-sight extinction of $A_\nu = 33$ mag. Assuming a distance of 7 kpc for the source, they estimated the interstellar extinction near the Galactic plane to be approximately 8 mag. Based on this, they concluded that the source must be experiencing significant circumstellar extinction. The study analyzed the Spectral Energy Distribution (SED) using their observations, as well as photometric data from various archives (2MASS, GLIMPSE-I, MSX, and IRAS databases). The result was a negative spectral index of -0.34 ± 0.24 for the non-thermal components, different from -0.8 reported some years earlier (Cohen et al., 2006). These results are also compared with a spectral index of -0.68 ± 0.01 reported by Pérez-Sánchez et al. (2013). In their study, they noticed that the spectral index varies substantially with the years. Characteristics of 2009 observations (Bains et al., 2009) as the non-thermal spectral index led to the conclusion that the source could have the presence of wind-shock interactions. Bains et al. (2009) agreed with Deacon et al. (2007), IRAS 15445-5449 appeared to be a remarkable object with unique properties.

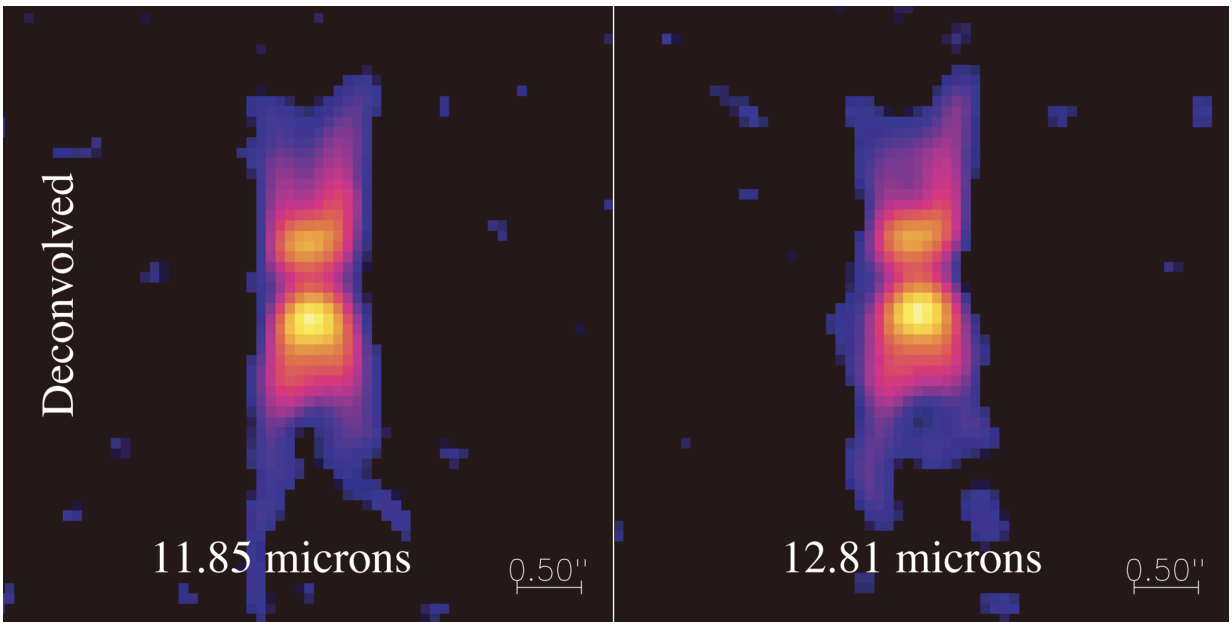

Figure 1.5: *First IR images of IRAS 15445-5449 obtained by VISIR/VLT at* 11.85 *and* 12.81 μm. *Adopted from Lagadec et al. (2011)*

It was not until 2011 that the first IR images of the source were published (Lagadec et al., 2011). Images were part of a catalog designed to image 93 post-AGB stars at mid-infrared. Their goal was to prove that these sources have emission of dusty structures in the inner part of the extended region. Observations were obtained by VISIR/VLT at 11.85 and 12.81 μm (see Figure 1.5), confirming earlier hypotheses about the structural characteristics of the source: IRAS 15445-5449 is a WF and post-AGB star with bipolar morphology and jets of material flowing from a dusty emission launching base.

Observations of ATCA (Australia Telescope Compact Array) in 2007 indicated the potential presence of a collimated magnetic field at its jets (Pérez-Sánchez et al., 2011). An analysis of water

maser polarization on the emitting region was performed to confirm it (Pérez-Sánchez et al., 2011). The upper limit for the magnetic field along the line-of-sight was estimated to be $|B_{||}| < 470$mG. A couple of years later, in 2012, IRAS 15445-5449 was observed again with ATCA, leading to the first resolved detection of a synchrotron jet towards a post-AGB star (Pérez-Sánchez et al., 2013). Observations of spatially resolved radio continuum emission were consistent with mid-IR images of 2011 (Lagadec et al., 2011). As discussed above, Pérez-Sánchez et al. (2013) recognized flux variations on the SED maps from three different epochs. They proposed that the flux variation could be interpreted as episodic shocks between high velocity wind (associated with synchrotron emission) and the slow AGB remnant wind.

New observations of IRAS 15445-5449 were performed with SINFONI/VLT, detecting the spatial distribution of H_2 (1-0) line (Pérez-Sánchez et al., 2018). Compared with the 2007 and 2012 H_2O distribution of 22 GHz water masers, there seems to be a correlation. Including dust continuum emission, the medium has conditions that favor the formation of H_2O in regions where H_2 re-forms. Molecule and dust grain formation theory establishes this type of interaction for dense clouds (Hollenbach et al., 2013). With H_2 line emission, a new systemic velocity was calculated to be $v_{sys} = -96.4 \pm 34$ km/s. This result is different from the systemic velocity calculated before using the OH line emission (Deacon et al., 2007). This result gives us a key to understanding the source kinematics.

There are many estimates for the distance to the source. First distance reported was 7 kpc, calculated assuming a flat galactic rotation model with a galactic center distance of 8.5 kpc and a circular rotation speed of 220 km/s (Deacon et al., 2007). It was not until 2014 that the first distance catalog for post-AGB stars was developed. The distance to IRAS 15445-5449 was calculated by modeling its SED with multiple blackbody curves; the distance reported in the catalog is 4.38 ± 0.69 kpc (Vickers et al., 2015). In 2018, when recalculating the systemic velocity with H_2 lines, the kinematic distances were estimated. For those observations, near and far distances are 5.4 ± 0.4 kpc and 8.5 ± 0.4 kpc, respectively (Pérez-Sánchez et al., 2018). Near distance is consistent with the error range of the SED method distance catalog. Here in this work, we will use the distance of ~ 4.4 kpc in calculations if necessary because it is the value most commonly used in the literature.

The following discussion is based entirely on the results of Khouri et al. (2021). In 2021, ALMA observations of 15 sources classified as WFs were performed. Their analysis focused on the characteristics of common envelope evolution in the circumstellar envelopes of this type of source. For IRAS 15445-5449, they detected the J=19-18 line of OCS (Carbonyl Sulfide) and the $O^{13}CS$ isotopologue. Also they observed ^{12}CO (J = 2 - 1) , ^{13}CO (J = 2 - 1) , $C^{18}O$ (J = 2 - 1), $C^{17}O$ (J = 1 - 0) transitions. The $^{17}CO/^{18}CO$ ratio is a good tracer of the initial stellar mass for post-AGB stars. This is because the abundance of ^{17}O is modified by a mixing process that is dependent on the initial stellar mass and takes place much before the AGB. Assuming optically thin emission and solar composition, they derived the initial stellar mass for IRAS 15445-5449 as $\lesssim 1.4$ $M_\odot$. With similar processes, they estimated the fraction of H_2 mass in the star as 0.55 $M_\odot$. The time scale since the beginning of ejection is determined assuming ballistic expansion

of the outflow. For this source, the time scale is reported as 110 yrs. Using molecular hydrogen mass and time scale, they estimate mass loss rate as 5×10^{-3} $M_{\odot}$/yr. For IRAS 15445-5449, contamination where found on ^{12}CO spectral lines, as the source is close to the galactic plane, lines were affected by large-scale Galactic CO contamination. They corrected that effect in the calculations of integrated line fluxes.

1.6 Aims of this thesis

IRAS 15445-5449 is a post-AGB star with a CSE and a bipolar morphology produced by jets of material being ejected at high velocities. Interferometry ALMA observations of the source are key to analyzing the base of the jet with better resolution. In this thesis, we will determine the spatial and kinematic distribution of molecular gas in the CSE of this source based on molecular line emission. The analysis of the different moment maps of the resolved emission would allow us to infer the sizes and velocity ranges of the molecular gas in emission. This information is the key input for non-LTE radiative transfer models, which will give more information about this archetype of post-AGB stars.

Chapter 2

Observations and Methods

2.1 ALMA observations

IRAS 15445-5449 was observed in August 2017 with the 12-m ALMA array on Cycle 4 of science observations with C40-7 configuration. Frequency band 7 ($\sim$ 294–345 GHz) was observed in four Spectral Windows (SPWs), see Table 2.1 for more details. For this configuration, observations were performed with 44 antennas reaching minimum and maximum baselines of 64 m and 3.6 km, respectively. The average integration time of observation was $\sim$ 671 seg pointing to RA = 15h 48m 19.39s and DEC = -54° $58'$ $20.62''$. In terms of resolution, three SPWs were set to low-spectral bandwidth (1938.48 MHz), while the remaining one was set to high-spectral bandwidth (282.2 kHz). Configuration and spectral setup were determined based on the science goal, looking for the detection of 321 GHz H_2O maser transition. Continuum and spectral line emission were detected in every SPW. Average of synthesized beam across the different SPWs is $0.075'' \times 0.064''$ with a position angle PA= 39.4°. The field of view was FOV= 17.876, estimated from the baselines. Data were calibrated using the Common Astronomy Software Applications (CASA) version 4.7. Amplitude and Phase calibrators utilized were respectively J1427−4206 and J1531−5108. After subtraction of continuum, channels with spectral line emission were split out and deconvolved individually using the CASA task *tclean*.

SPW	Range [GHz]	Center [GHz]	Resolution [kHz]
25	321.15 - 321.62	321.39	282.22
27	318.22 - 320.09	319.16	1938.48
29	329.84 - 331.71	330.78	1938.48
31	331.73 - 333.60	332.67	1938.48

Table 2.1: *Frequency spectral window specifications for the 2017 observations of IRAS 15445-5449, including the frequency range, central frequency, and resolution of each spectral window.*

2.2 Spectral Processing

2.2.1 Spectral Line Identification

The identification of the detected lines was done using CASA tools for spectral line observations. Specifically, CASA queries the Cologne Database for Molecular Spectroscopy (CDMS) (Müller et al., 2001) to identify molecular species that could be detected in the (sub)-millimeter wavelength range. Given a data cube, the identification process with CASA starts by navigating through the different channels of the cube to identify and select the region of emission. Once selected, it is possible to extract the spectrum with the spectral profile tool. For every SPW, the mean emission is shown (but could be changed to median, sum, or flux density). CASA allows for overlaying the spectral lines of the CDMS in the emission profile. Given some filters, the line overlay tool displays a list of possible molecular lines. It is possible to select and display individual lines or the complete set of species from the list. Filters for identification include the type of astronomical source; in this case, the source category selected was AGB/PPN/PN. Also, it is necessary to filter for a range of frequencies to search. For every SPW, ranges were selected, taking the individual emission for the brightest lines.

Figure 2.1: *CASA identification tool. The mean emission of* ^{13}CO *(3 - 2) line is displayed. The bottom right panel shows the list of molecules queried with the bottom left filters. Filters include a range of frequencies between* 330.5 *GHz and* 330.8 *GHz, a velocity shift of* -90 *km/s, and an astronomical filter searching for molecules in AGB/PPN/PN. The* ^{13}CO *(3 - 2) species was selected and displayed overlapped with the spectral emission, showing a correct identification.*

Molecular lines were determined from the filtered list, looking for the simplest molecules and those that had the lowest upper energy. The information of the identified molecular species and their transitions can be found in Table 3.2. The brightest line detected was the ^{13}CO (J = 3 - 2) transition. Sulfur dioxide (SO_2) transitions were also identified (see Figure 2.2). The systemic velocity was previously estimated using the velocity of the H_2 emission line (Pérez-Sánchez et al.,

2018). However, we noticed that the line plotted was shifted from the center of the ^{13}CO (J = 3 - 2) spectral line. This led us to use −90 km/s as systemic velocity previously defined as an initial parameter, looking for a better fit of the ^{13}CO (J = 3 - 2) spectral line. Based on that, we perform a detailed analysis of the systemic velocity of the source later in this work. We assumed this center of velocity to identify the rest of the spectral lines on the different SPWs.

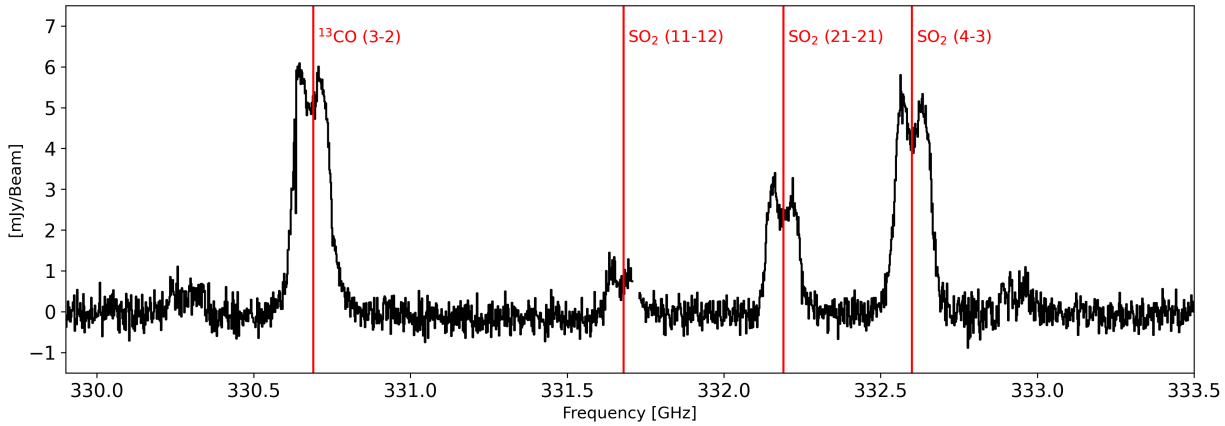

Figure 2.2: *Identified spectral lines in different SPWs of the ALMA data for IRAS 15445-5449. The black step line represents the main emission of the ALMA data cubes. In red, the ^{13}CO (3 - 2) emission line and three different SO_2 transitions (SO_2 ($11_{6,6}$ - $12_{5,7}$), SO_2 ($4_{3,1}$ - $3_{2,2}$), and SO_2 ($21_{2,20}$ - $21_{1,21}$)).*

From the lines identified, we focus our analysis on the emission lines detected on the upper side of the frequency range. Unfortunately, the SO_2 (J_{K_a,K_c} = $11_{6,6}$ - $12_{5,7}$) line is located on the edges of two different SPWs (See top of Figure 2.2). It was found that a part of the emission was cut off. It is difficult to give information for this type of line because it needs more extensive treatment, and the error may be higher. This leaves three available lines with valuable information about gas distribution on IRAS 15445-5449, and these will be the ones we will focus on in this work.

2.2.2 Preparation of Individual Spectral Line Cubes

ALMA data cubes require a high amount of computational resources. To optimize their use, the original data cube was cropped according to spatial and spectral limits that we will define below. For each line, we selected specific frequency or velocity channels (see Table 2.2), and spatial ranges in RA/DEC that fully cover the emission. The spatial ranges are RA: from 15h 48m 19.01s to 15h 48m 19.78s and DEC: from −54 58′ 23.46″ to −54 58′ 16.81″.

Each spectral line was then extracted into an individual spectral cube. This approach not only reduces data storage requirements but also allows us to define an individual velocity system for each spectral line. Frequency values were converted to radial velocities, centering each system at the central velocity defined before (−90 km/s). The black step line in Figure 2.3 shows the SO_2 (J_{K_a,K_c} = $4_{3,1}$ - $3_{2,2}$) emission line within our selected channel range, with frequency and velocity displayed as the upper and lower x-axis labels, respectively.

Lines	Frequency Range (GHz)	Velocity Range (km/s)
^{13}CO (J = 3 - 2)	330.39 – 331.01	-385.09 – 179.96
SO_2 (J_{K_a,K_c} = $4_{3,1}$ - $3_{2,2}$)	332.29 – 332.86	-321.52 – 192.72
SO_2 (J_{K_a,K_c} = $21_{2,20}$ - $21_{1,21}$)	331.96 – 332.43	-309.49 – 113.70

Table 2.2: *Selected frequency and velocity ranges for each spectral line, from which the data cubes were extracted individually.*

2.2.3 Fitting Spectral Lines

Fitting spectral lines is essential to derive mathematical models that provide quantitative information about their physical properties. Due to their shape, basic models for fitting spectral lines are normally Gaussian. As our spectral lines have a two-peak profile, a two-Gaussian model will be applied. Fitting was performed using Python with the 'lmfit' library and its Gaussian model. Given the data of a spectral line, the fitting process starts by choosing appropriate channels to work on. It means, channels of the spectrum have to be in a region where emission is fully covered and includes some noise, but ensuring that emission contributes mostly to the information. The green region on Figure 2.3 is the range of channels selected for the SO_2 (J_{K_a,K_c} = $4_{3,1}$ - $3_{2,2}$) line. For fitting computational methods, giving good initial parameters to the model is essential. For a model defined as the sum of two Gaussians, six initial parameters are needed: the amplitude, the central value, and the width of each component. A Python script was built to perform a process in order to obtain the best parameters.

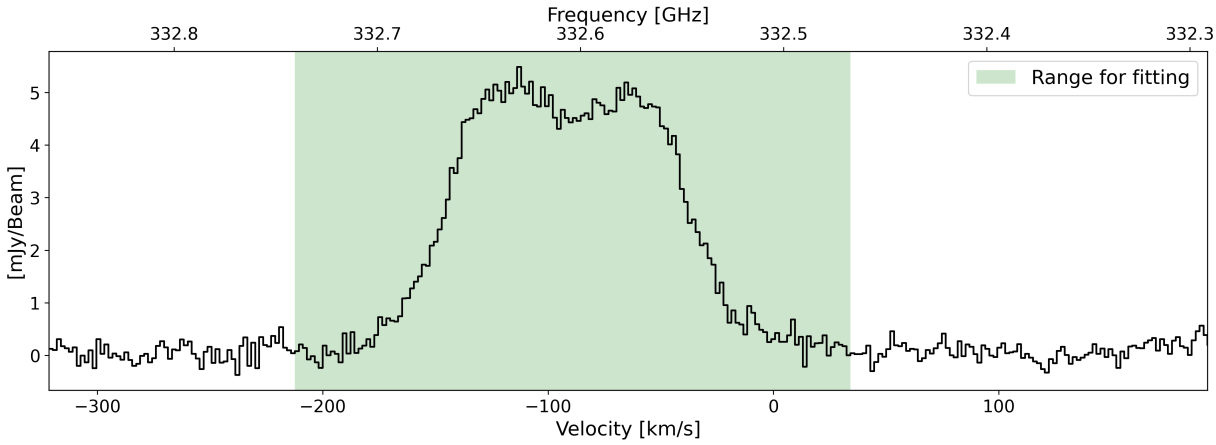

Figure 2.3: *Mean line emission of SO_2 ($4_{3,1}$ - $3_{2,2}$) before individual extraction with the frequency axis labeled at the top and the velocity axis labeled at the bottom. The green shaded region indicates the range of channels selected for the computational fitting.*

First, it determines the center of the line to divide the emission into two regions. For every region (left and right), initial parameters are estimated. The center is estimated with the

x-value that corresponds to the maximum y-value for both regions. Amplitude is defined as the maximum y-value. And the width is estimated as the length of 30 channels on both sizes, as an approximation. The library 'lmfit' is in charge of running a Gaussian model to estimate best-fit parameters. The parameters we are interested in are the center of the line and its components, their full half-width maximum, and amplitude. It is difficult to define the exact center of the line, so the Python script iterates at different values near −90 km/s (as we determined the central velocity at that point). Then, with 'lmfit' is easy to obtain the chi-square value for every iteration of the center. Based on that, parameters with the minimum value of chi-square are selected.

Given the broad nature of the lines detected in IRAS 15445-5449, our model was built to fit the lines as the sum of two Gaussian components, with the six initial parameters determined before (three for the left region and three for the right region of the emission).

2.3 Continuum Emission

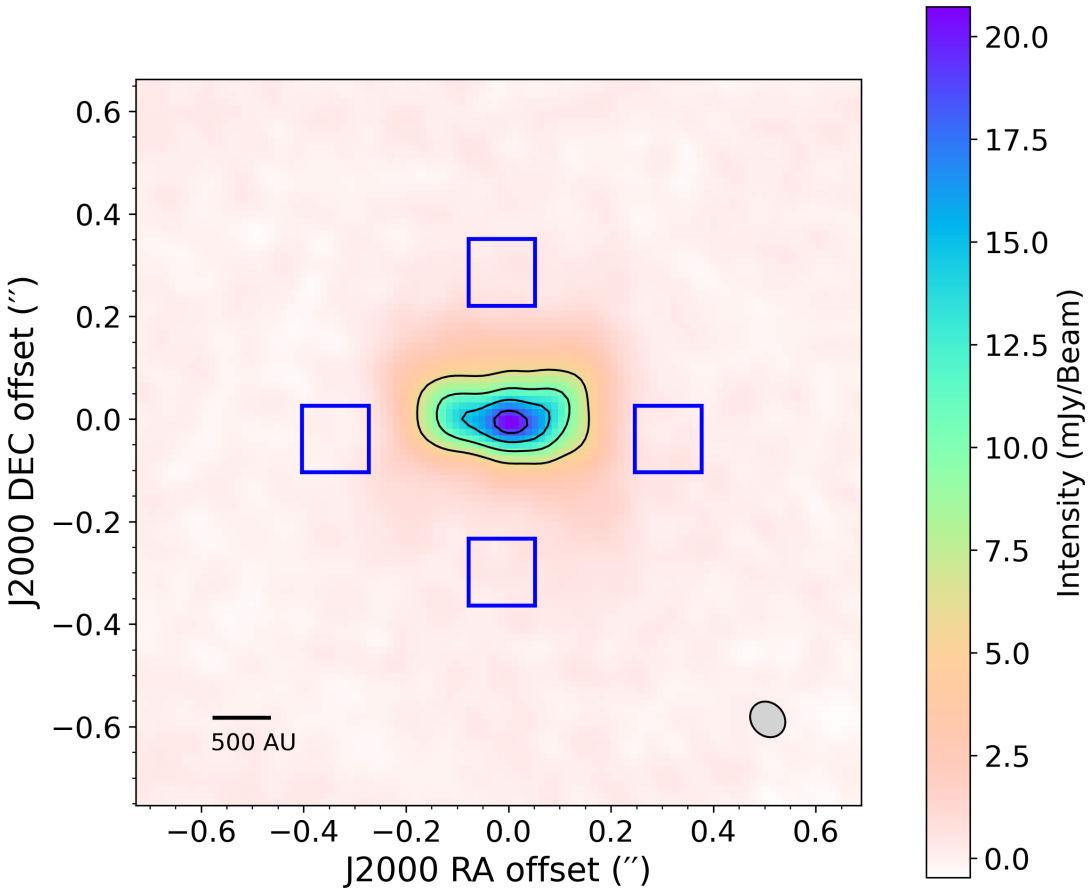

Figure 2.4: *Dust continuum emission map. The four equal-sized boxes indicate the regions used to estimate the RMS, calculated as the mean standard deviation of the values within each box. The synthesized beam is shown in the bottom right corner. The size scale of* 500 *AU, calculated assuming a distance of* 4.4 *kpc to the source, is shown in the bottom left corner. The origin of coordinates is placed at the brightest point of the emission.*

From the observations, it is possible to extract an ALMA continuum emission map using the *tclean* task in CASA. As observations were performed in different SPWs, the extraction process was executed using the "specmode = 'mfs'" [1] option to obtain continuum emission with only one output image channel. The final result is shown in Figure 3.1. The map of the continuum emission was made considering all the line-free channels within the spectral range observed. The RMS was estimated using the mean standard deviation of 4 equal-sized boxes located on the background around the emission (See Figure 2.4).

2.4 Moment Maps Methods

Dimensional moment maps are the best way to present data cubes of line emission. A moment map is a projection of data cubes to a 2-dimensional space after masking noise. The definition of the first three moment maps is:

$$M_0 = \int I_\nu d\nu \tag{2.1}$$

$$M_1 = \frac{\int \nu I_\nu d\nu}{M_0} \tag{2.2}$$

$$M_2 = \frac{\int I_\nu (\nu - M_1)^2 d\nu}{M_0} \tag{2.3}$$

Every moment map gives us information about the distribution of molecular gas in the emitting region. Moment 0 represents the integrated intensity over the spectral line, i.e, the sum of the emission along the frequency axis. Moment 1 represents the intensity-weighted velocity of the spectral line. Moment 2 is the velocity field and represents weighted velocity dispersion about the mean. For data cubes, Equation 2.1, 2.2, and 2.3 have to be applied on every pixel along the frequency axis to make a 2-dimensional representation of the cube based on the moments definition.

There are different software tools, such as Python with the 'astropy' library or CASA with the 'immoment' task, that can build moment maps from spectral cubes. The process to obtain a moment map is similar for both options. First, it is necessary to mask noise in the spectral cube in order to correctly apply the definition of moment maps and reduce the bias. As noise is not part of the real emission, the process involves identifying and isolating the region of interest that contains the real signal. In case of spectral cubes, only frequency channels with emission above 3σ were included, focusing on the spectral line and excluding channels dominated by noise. For intensity levels, a threshold must be defined. The noise level limit was selected based on the 3σ contour level of intensity, but also trying to exclude low-intensity values that may correspond to noise rather than true spectral emission. Once the emission region was selected, Moment 0 and Moment 2 maps were computed for the ^{13}CO (J = 3 - 2) line and the brightest lines detected of SO_2.

[1] 'mfs' means Multi-Frequency Synthesis and is a method where data is mapped to a single broadband uv-grid, and then imaged.

Chapter 3

Line Emission and Dust Continuum Results

3.1 Dust Continuum

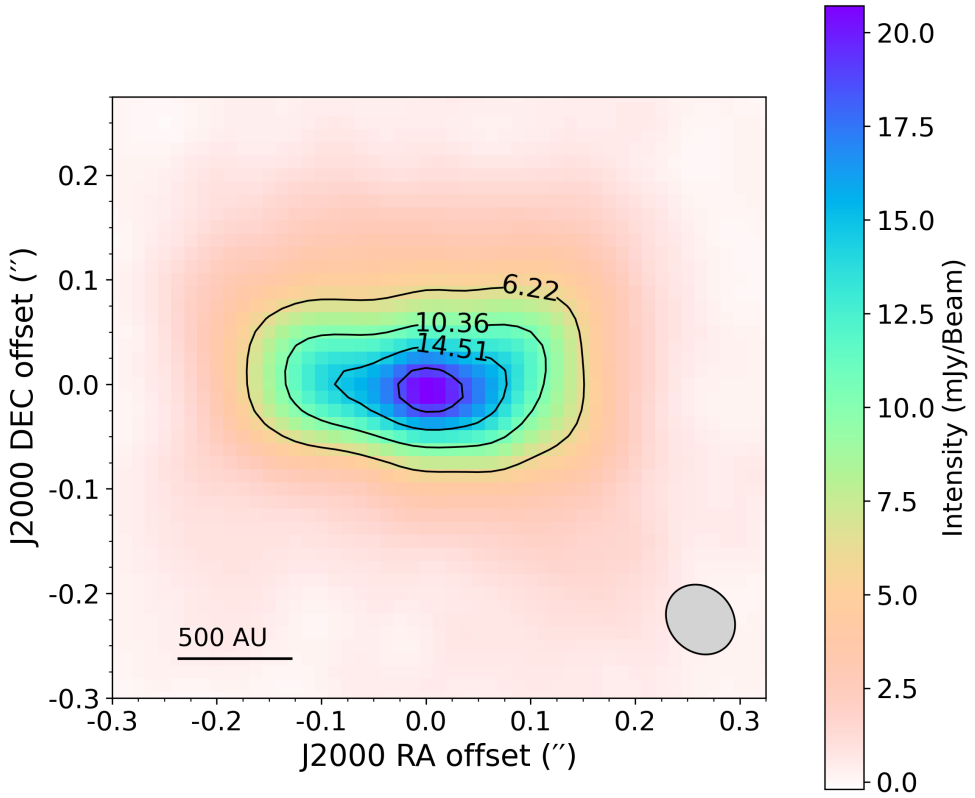

Figure 3.1: *Dust continuum emission of IRAS 15445-5449. Black contours represent* 0.3, 0.5, 0.7, *and* 0.9 *fractions of the peak flux density. The synthesized beam is shown in the bottom right corner. The size scale of* 500 *AU, calculated assuming a distance of* 4.4 *kpc to the source, is shown in the bottom left corner. The origin of coordinates is placed at the brightest point of the emission.*

The Figure 3.1 shows the spatial distribution of the dust emission. The peak of the emission is 20.3 mJy/beam, and we set the origin of the reference system in those coordinates. The RMS calculated is 0.3 mJy. The continuum emission outlines a box-like structure, elongated parallel to the RA axis. The size of the structure is 0.33″ along the major axis (RA), and 0.18″ along the minor axis (DEC) at 6.22 mJy/Beam intensity contour level. The Synthesized beam is 0.074″ × 0.064″ oriented along PA= 43°. Based on the beam size, the emission is resolved.

3.2 Molecular Emission

3.2.1 PV diagrams and emission structure.

The high-quality data allow us to use the ALMA data cubes to study the properties of the spectral lines detected towards IRAS 15445-5449. In that sense, good visualization is the next step when characterizing the emission from a source. Figures 3.2 and 3.3 are top and side views, respectively, of the ALMA data cube for the three spectral lines. These types of diagrams are also known as Position-Velocity (PV) diagrams. PV diagrams help to visualize how the velocity of a particular spectral line varies along position axes.

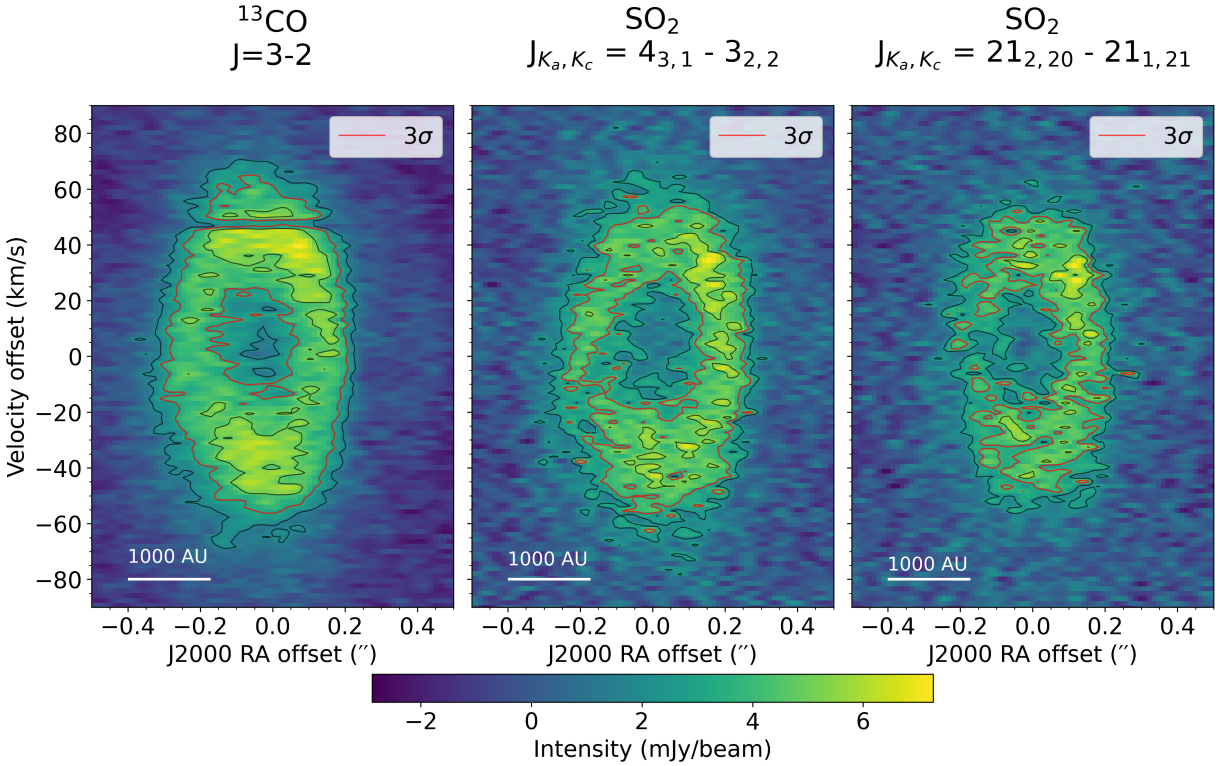

Figure 3.2: *PV diagram along the RA axis (top view of the ALMA data cube) for the* ^{13}*CO* (3 - 2)*,* SO_2 ($4_{3,1}$ - $3_{2,2}$)*, and* SO_2 ($21_{2,20}$-$21_{1,21}$) *line emission (left to right). Black contours correspond to* 2σ *and* 4.2σ*, while the red contour indicates* 3σ *of the flux intensity. The velocity axis is centered on* -90 *km/s. The size scale of* 1000 *AU, calculated assuming a distance of* 4.4 *kpc to the source, is shown in the bottom left corner.*

Figure 3.2 shows the PV cut along the RA axis for the three lines analyzed. The molecular gas in emission is distributed over a ring-scale structure. In the case of the ^{13}CO (J = 3 - 2), the velocity range along the y-axis indicates that the brightest part of the emission is generated from molecular gas moving between 25 km/s and 60 km/s. The same ring-like structure is seen in the PV cuts of the SO_2 lines. The emission outlines a similar velocity distribution to the ^{13}CO (J = 3 - 2), with a peak of emission at $\approx$ 30 km/s. However, the SO_2 emission traces an incomplete

ring-like structure, as the emission intensity changes from below to above 3σ along the RA for the lower velocities.

The emission above 3σ arises from an ellipsoid structure with inner and outer radii. Sizes are presented in Table 3.1. They were estimated using the mean value of four measurements over 3σ contours in the RA axis. Assuming a distance to the source of 4.4 kpc (Vickers et al., 2015), sizes on astronomical units could be estimated on average as $\sim$ 1000 AU for the outer radius and $\sim$ 570 AU for the inner radius for the three emission lines. In this case, the zero of the velocity corresponds to -90 km/s, as it was the systemic velocity previously defined.

The molecular gas region traced by the peak of the emission lines is moving at high velocities. The brightest regions are located in the red and blue shifted parts of the emission, which is especially noticeable in the ^{13}CO (J = 3 - 2) line. The low velocity component of the emission arises from two separate regions in RA. The cavity of both SO_2 transitions is bigger and less differentiated than that of the ^{13}CO (J = 3 - 2) line. In that sense, it seems that the ellipse is busted on the negative side of the RA offset of both SO_2 transitions.

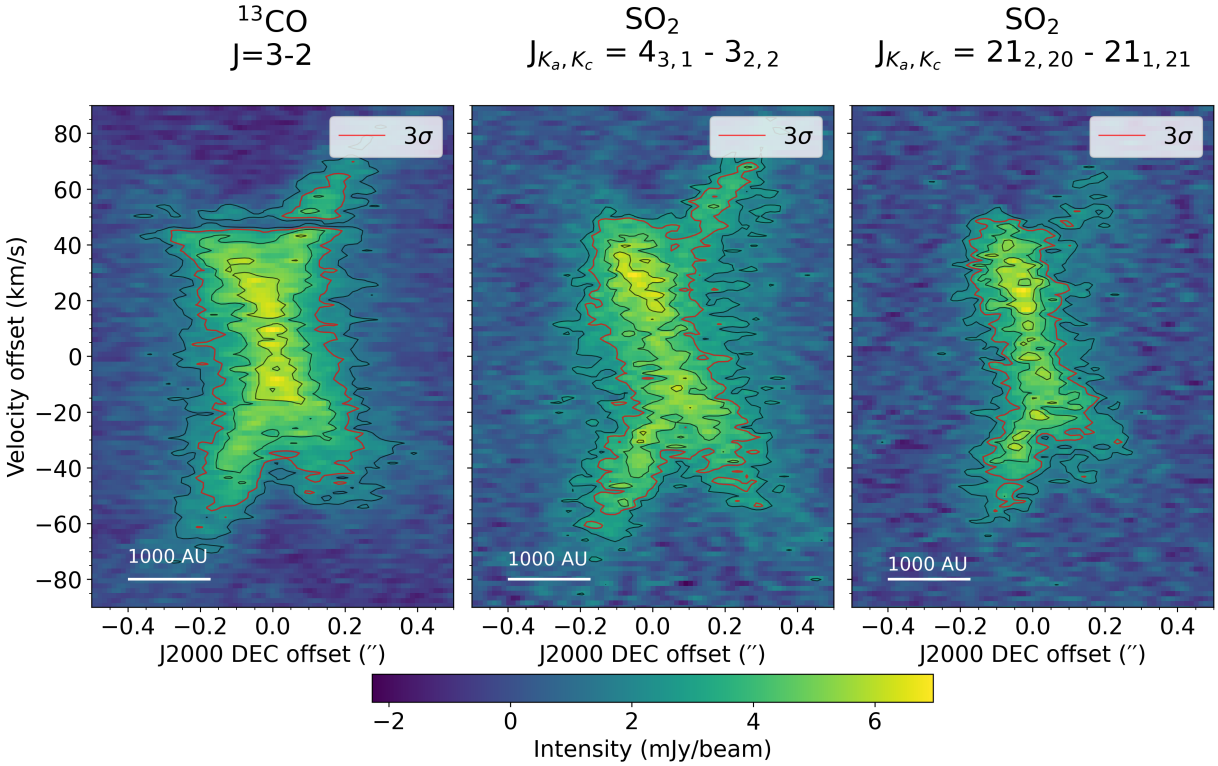

Figure 3.3: *PV diagram along the DEC axis (side view of the ALMA data cube) for the ^{13}CO (3 - 2), SO_2 ($4_{3,1}$ - $3_{2,2}$), and SO_2 ($21_{2,20}$-$21_{1,21}$) line emission (left to right). Black contours correspond to 2σ, 4.2σ, and 5.5σ, while the red contour indicates 3σ of the flux intensity. The velocity axis is centered on -90 km/s. The size scale of 1000 AU, calculated assuming a distance of 4.4 kpc to the source, is shown in the bottom left corner.*

Figure 3.3 shows the PV cut along the DEC axis for the three lines analyzed. Similar to the PV cut along the RA axis, the structure outlined by the three lines is comparable in shape, up to

the 3σ level of the emission. Moreover, the velocity range covered by the three transitions is also in agreement.

Emission presents an X-shape structure with velocity ranges and DEC sizes presented in Table 3.1. Using the distance of 4.4 kpc, the estimation of the mean size for the three line emission over DEC is $\sim$ 1600 AU. Concerning the sizes at the 3σ level, the ^{13}CO (J = 3 - 2) line shows that the brightest emission is confined to a narrow region along the DEC axis, and extends over a wide velocity range between -30km/s to 30 km/s. Meanwhile, for both SO_2 transitions, the brightest emission is concentrated around 30 km/s. X-shape is less differentiated and emission is smaller for the SO_2 ($J_{K_a,K_c} = 21_{2,20}$-$21_{1,21}$) line compared with the other two.

Lines	RA size Inner Radii ($''$)	RA size Outer Radii ($''$)	DEC size ($''$)	Velocity Range (km/s)
^{13}CO (J = 3 - 2)	0.13	0.24	0.47	-70 – 70
SO_2 ($J_{K_a,K_c} = 4_{3,1}$ - $3_{2,2}$)	0.15	0.23	0.41	-60 – 70
SO_2 ($J_{K_a,K_c} = 21_{2,20}$-$21_{1,21}$)	0.11	0.18	0.29	-50 – 60

Table 3.1: *Sizes and velocity ranges, derived from PV diagrams for all emission lines.*

3.2.2 Emission lines

Based on the methodology, emission lines were detected on every SPW. Brightest lines include three different transitions of SO_2 and a transition of ^{13}CO (J = 3 - 2). Detected molecular transitions from spectral lines on IRAS 15445-5449 due to ALMA observations are shown in Figure 2.2. Strongest spectral lines are wide and show a two-peaked morphology, indicating that material in the source is moving at high velocities. Some weak lines are also present on the spectrum, but they will not be analyzed in this work. Information on the identified lines and their transitions can be found in Table 3.2.

Species	Transition QNs	Frequency (GHz)	Energy Upper (K)
^{13}CO ($\nu = 0$)	3-2	330.59	31.73
SO_2 ($\nu = 0$)	11 (6,6) - 12 (5,7)	331.58	148.95
SO_2 ($\nu = 0$)	4 (3,1) - 3 (2,2)	332.50	31.29
SO_2 ($\nu = 0$)	21 (2,20) - 21 (1,21)	332.09	219.52

Table 3.2: *Spectroscopic information and Quantum Numbers (QNs) for different molecule transitions detected in IRAS 15445-5449. Information from CDMS (Müller et al., 2001).*

The spectral line emission for ^{13}CO (J = 3 - 2), SO_2 ($J_{K_a,K_c} = 4_{3,1}$ - $3_{2,2}$) and SO_2 ($J_{K_a,K_c} = 21_{2,20}$-$21_{1,21}$) transitions from ALMA data are shown on a black line in Figures 3.4, 3.7 and

3.10 respectively. The emission lines are broad and outline a two-peak profile. The velocity range covered indicates that part of the material is flowing at high velocities. As described before, a two-component Gaussian is used to fit the spectral lines. Blue and red dashed lines are both components of the movement (see also Table 3.3 for parameter information). The purple solid line is the sum of both Gaussian models, producing our model representation of the two-picked spectral line. The spectral line covers a significant width of almost 200 km/s, 170 km/s and 145 km/s for ^{13}CO (J = 3 - 2), SO_2 (J_{K_a,K_c} = $4_{3,1}$ - $3_{2,2}$), and SO_2 (J_{K_a,K_c} = $21_{2,20}$-$21_{1,21}$) respectively (see Table 3.3 for velocity ranges). Around −40 km/s, the ^{13}CO (J = 3 - 2) spectra show a narrow absorption feature, most likely associated with molecular CO along the line-of-sight in the Galaxy plane.

The blue component of ^{13} CO line is higher and wider than the red component, even if the emission peaks appear to be symmetric. For SO_2 (J_{K_a,K_c} = $4_{3,1}$ - $3_{2,2}$), both the model and the emission appear to have a structure with two peaks equidistant from the center and with similar heights. On the other hand, the red component of SO_2 (J_{K_a,K_c} = $21_{2,20}$-$21_{1,21}$) is higher than the blue component in both the model and the emission.

Lines	Central Velocity (km/s)	Velocity Range (km/s)	Blue Component μ (km/s)	Blue Component σ (km/s)	Red Component μ (km/s)	Red Component σ (km/s)
^{13}CO (J = 3 - 2)	−85.8	−200 – 0	−115.10	27.59	−56.50	23.58
SO_2 (J_{K_a,K_c} = $4_{3,1}$ - $3_{2,2}$)	−88.8	−180 – −10	−118.99	23.57	−58.70	21.62
SO_2 (J_{K_a,K_c} = $21_{2,20}$-$21_{1,21}$)	−88.3	−160 – −15	−116.05	20.99	−60.50	17.83

Table 3.3: *Results of the two-Gaussian model fits for each spectral line, including the central velocity, velocity ranges, and the parameters of the blue and red components.*

3.2.3 The ^{13}CO (J = 3 - 2) line emission

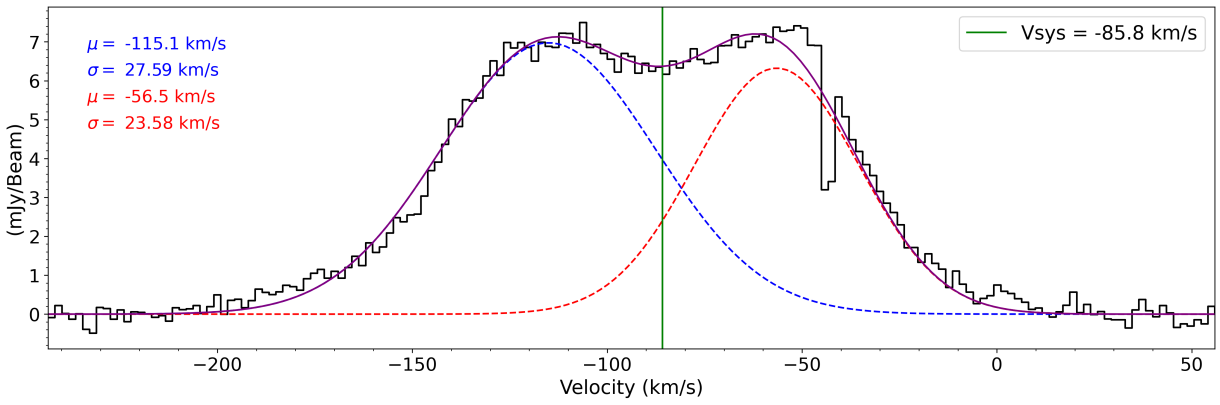

Figure 3.4: *Mean ^{13}CO (3 - 2) line emission is shown as a black line. Blue and red dashed lines represent the two velocity components, with their parameters indicated in the upper left corner. The purple solid line shows the sum of the two-Gaussian model, providing the best fit to the emission. The green vertical line indicates the central velocity of the model.*

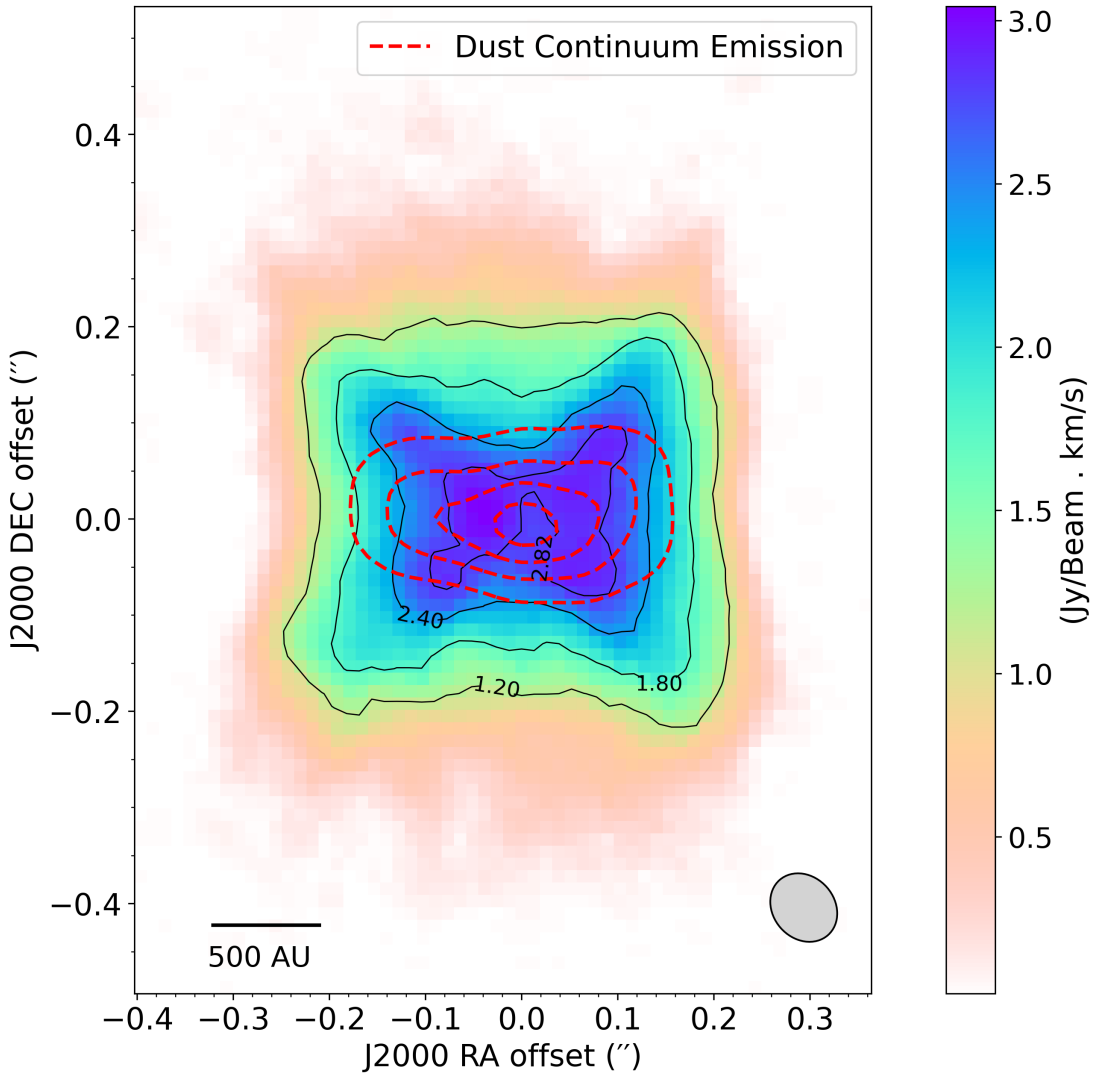

Figure 3.5: *Moment 0 (integrated intensity map) of the ^{13}CO (3 - 2) line emission. Red contours trace the dust continuum emission, while black contours represent* 0.4, 0.6, 0.8, *and* 0.9 *fractions of the peak line intensity. The synthesized beam is shown in the bottom right corner. A scale bar of* 500 *AU, calculated assuming a distance of* 4.4 *kpc to the source, is shown in the bottom left corner. The coordinate origin is set at the brightest point of the continuum emission, as in Figure 3.1.*

Computed moment 0 for ^{13}CO (J = 3 - 2) line is presented in Figure 3.5. The integrated line emission structure outlines a boxy structure, brighter in the center. Due to the beam size, the structure is resolved. Black contours were displayed for 0.4, 0.6, 0.8, 0.9 fractions of the peak intensity of flux emission. Maximum value of integrated intensity is 3.04 Jy/Beam · km/s, located at (−39 mas, 13 mas) for RA and DEC offsets respectively. The peak is offset 0.041″ from the origin of coordinates. Same dust continuum emission contours of Figure 3.1 are plotted in red dashed lines as a reference for sizes. For a better understanding of sizes, assuming a distance to the source of 4.4 kpc, the dimensions of the structure were calculated and are shown in both ″ and AU, see Table 3.4.

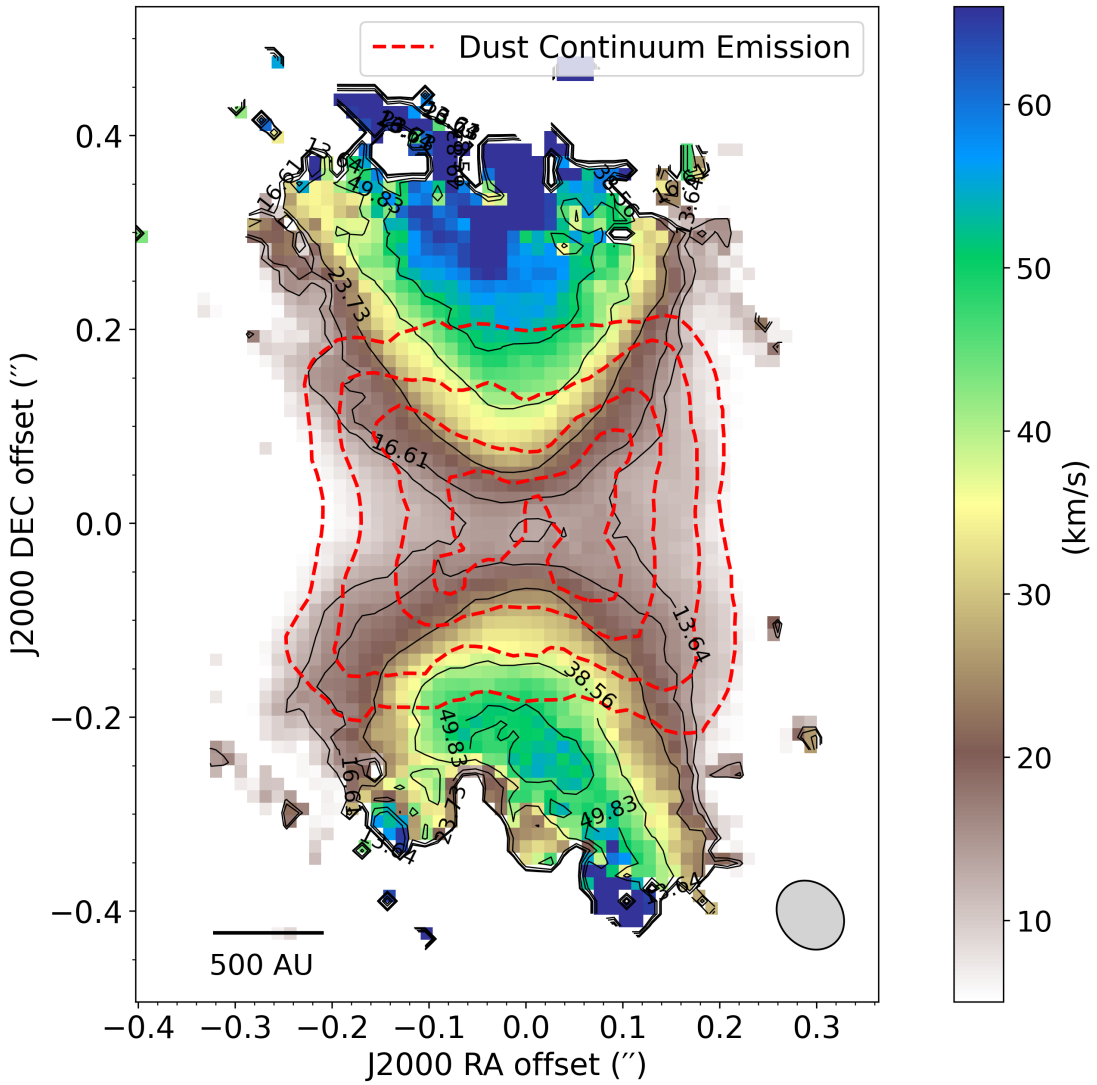

Figure 3.6: *Moment 2 (kinematic distribution map) map of the* ^{13}CO *(3 - 2) emission. Red contours trace the integrated intensity (Moment 0; see black contours in Fig. 3.5), while black contours represent* 0.23, 0.28, 0.40, 0.65, 0.84, *and* 0.99 *fractions of the maximum velocity. The synthesized beam is shown in the bottom right corner. A scale bar of* 500 *AU, calculated assuming a distance of* 4.4 *kpc to the source, is shown in the bottom left corner. The coordinate origin is set at the brightest point of the continuum emission, as in Figure 3.1.*

Moment 2 for ^{13}CO (J = 3 - 2) line is presented in Figure 3.6. The presence of a collimated bipolar structure traced by molecular gas moving at high velocities ($\sim$ 40 km/s) is evident. However, the most significant emission is within the red contours, which are the same as those in Figure 3.5, representing the spatial distribution of the gas. The central part of the kinematic distribution is the contribution of the slow wind that corresponds to velocities below the 24 km/s contour or brown region. The high-velocity outflows are shown in yellow and green regions (inside red contours) corresponding to velocities between 24 km/s and 50 km/s. The length of the yellow region between the two outermost red contours is approximately 0.28″ along the RA axis. Taking a 4.4 kpc distance to the source, the length is 1227 AU.

3.2.4 The SO_2 (J_{K_a,K_c} = $4_{3,1}$ - $3_{2,2}$) line emission

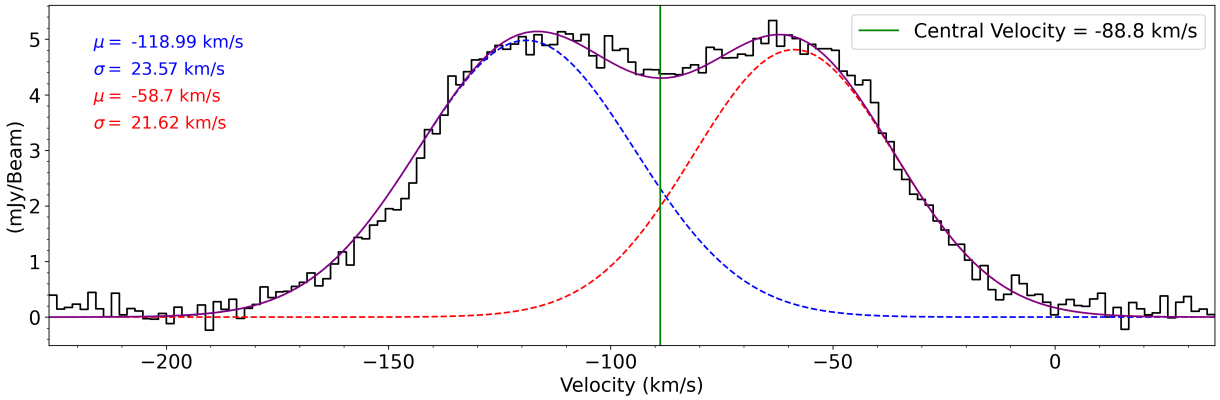

Figure 3.7: *Mean SO_2 ($4_{3,1}$ - $3_{2,2}$) line emission is shown as a black line. Blue and red dashed lines represent the two velocity components, with their parameters indicated in the upper left corner. The purple solid line shows the sum of the two-Gaussian model, providing the best fit to the emission. The green vertical line indicates the central velocity of the model.*

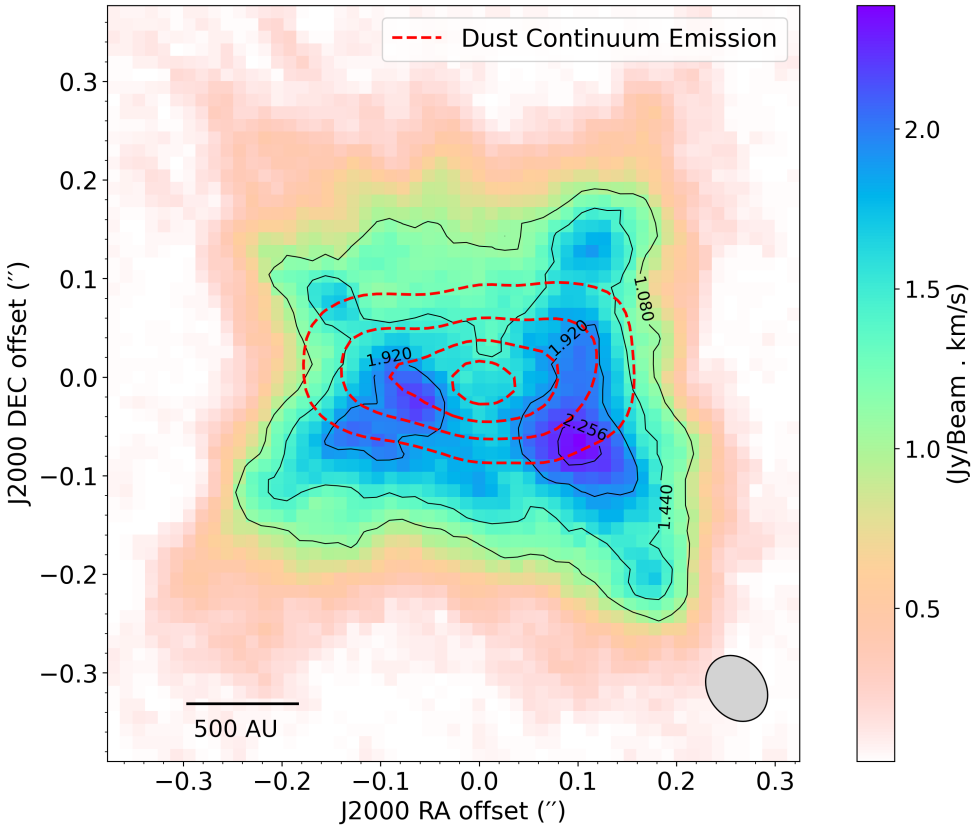

Figure 3.8: *Moment 0 (integrated intensity map) of the SO_2 (J_{K_a,K_c} = $4_{3,1}$ - $3_{2,2}$) line emission. Red contours trace the dust continuum emission, while black contours represent* 0.45, 0.6, 0.8, *and* 0.94 *fractions of the peak line intensity. The synthesized beam is shown in the bottom right corner. A scale bar of* 500 *AU, calculated assuming a distance of* 4.4 *kpc to the source, is shown in the bottom left corner. The coordinate origin is set at the brightest point of the continuum emission, as in Figure 3.1.*

Moment 0 of SO_2 (J_{K_a,K_c} = $4_{3,1}$ - $3_{2,2}$) is presented in Figure 3.8. A resolved structure is shown, featuring two brighter regions of integrated emission on the sides of the dust contours. The maximum value for integrated intensity is 2.38 Jy/Beam · km/s located at (0.104″,−0.065″) for RA and DEC offsets, respectively. Black contours represent 0.45, 0.6, 0.8, 0.94 fractions of the integrated emission maximum value. 1.080 Jy/Beam · km/s is the intensity value from which we define significant emission. The mean size of the structure was measured around that contour, see Table 3.4. The peak of intensity is offset from the center by 0.12″.

Moment 2 of SO_2 (J_{K_a,K_c} = $4_{3,1}$ - $3_{2,2}$) emission line is presented in Figure 3.9. The structure represents the kinematic distribution of the emission as a collimated bipolar structure with velocities between 10 km/s and 50 km/s. Red contours, identical to the black contours in Figure 3.8, delineate the spatial extent of the significant emission. Inside red contours, we can define brown pixels as areas of slow wind ($v \sim 20$ km/s); on the other hand, green pixels are tracing the high-velocity outflow areas ($v \approx 40$ km/s). The size of the yellow region on the RA axis is ~ 0.28 arcsec for velocities between 23.44 km/s and 33.52 km/s.

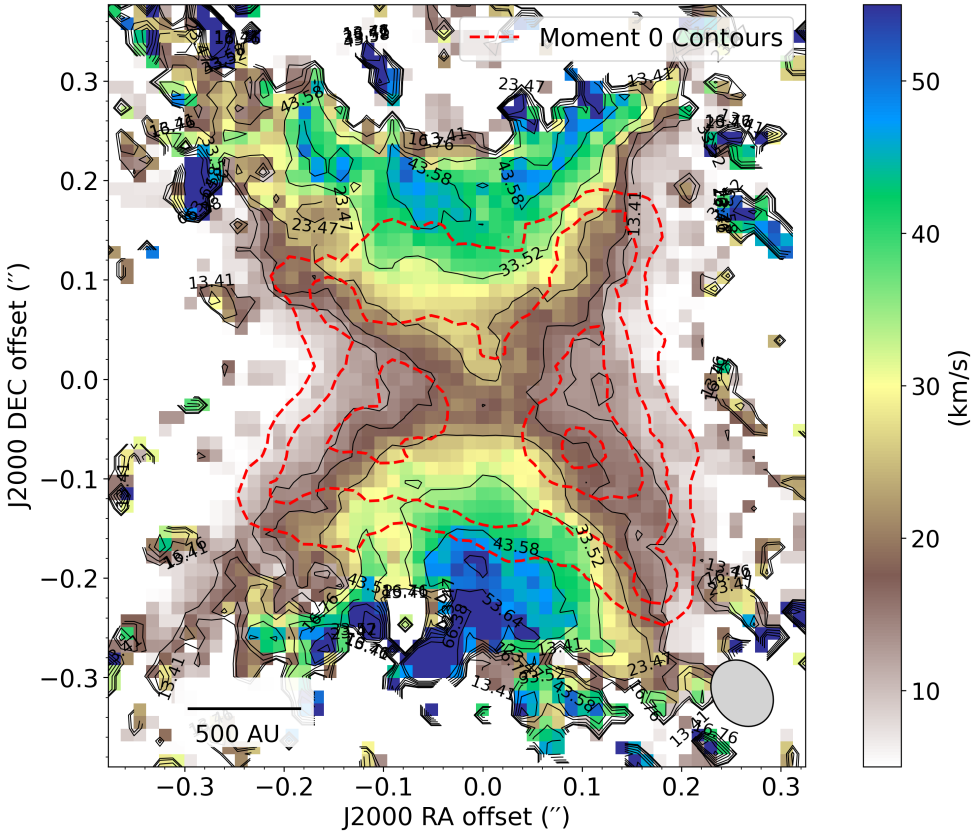

Figure 3.9: *Moment 2 (kinematic distribution map) of the SO_2 ($4_{3,1}$ - $3_{2,2}$) emission. Red contours trace the integrated intensity (Moment 0; see black contours in Fig. 3.5), while black contours represent* 0.23, 0.28, 0.40, 0.65, 0.84, *and* 0.99 *fractions of the maximum velocity. The synthesized beam is shown in the bottom right corner. A scale bar of* 500 *AU, calculated assuming a distance of* 4.4 *kpc to the source, is shown in the bottom left corner. The coordinate origin is set at the brightest point of the continuum emission, as in Figure 3.1.*

3.2.5 The SO_2 (J_{K_a,K_c} = $21_{2,20}$-$21_{1,21}$) line emission

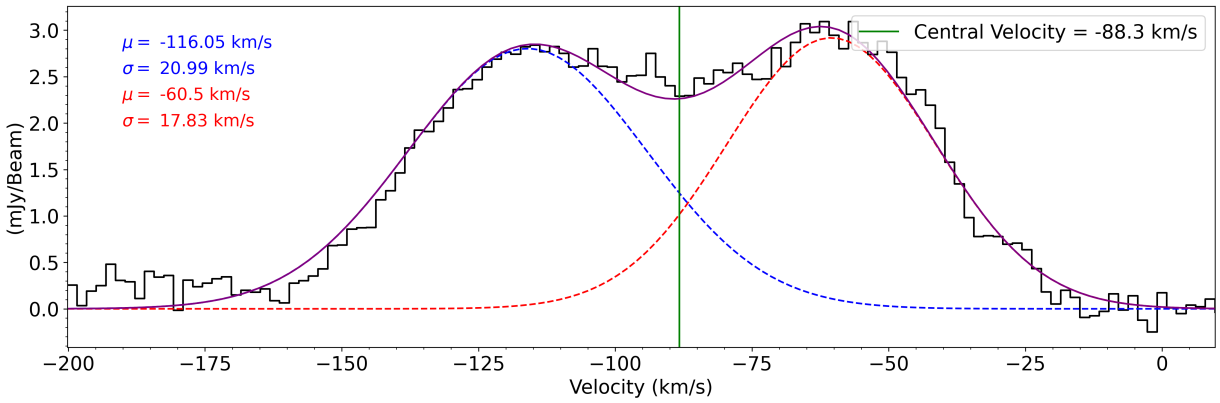

Figure 3.10: *Mean SO_2 ($21_{2,20}$-$21_{1,21}$) line emission is shown as a black line. Blue and red dashed lines represent the two velocity components, with their parameters indicated in the upper left corner. The purple solid line shows the sum of the two-Gaussian model, providing the best fit to the emission. The green vertical line indicates the central velocity of the model.*

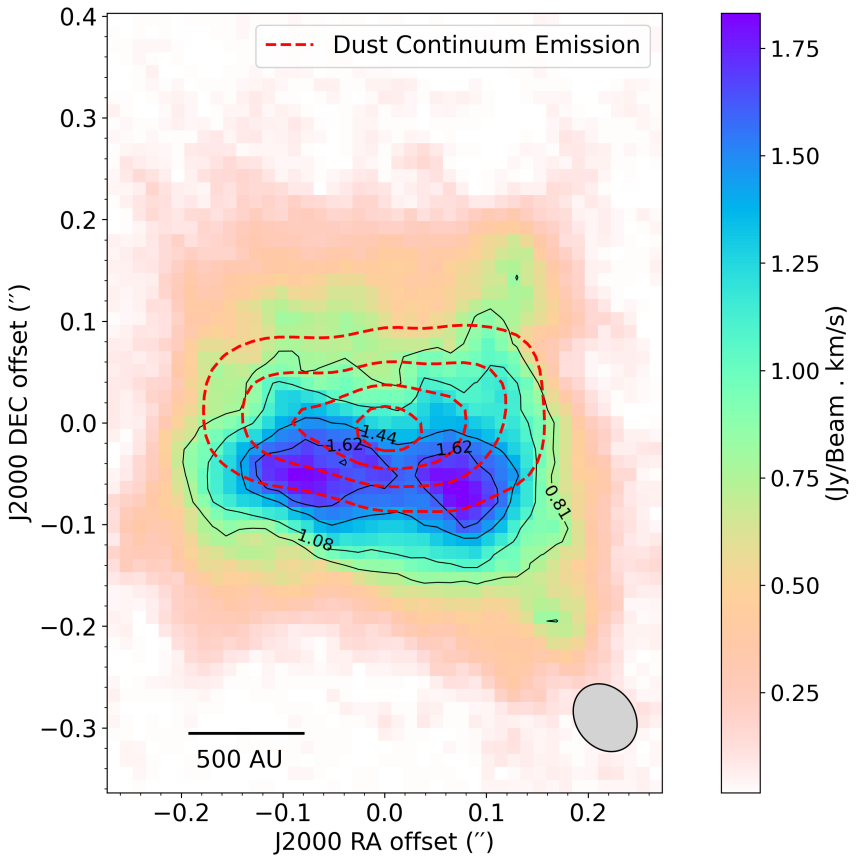

Figure 3.11: *Moment 0 (integrated intensity map) of the SO_2 (J_{K_a,K_c} = $21_{2,20}$-$21_{1,21}$) line emission. Red contours trace the dust continuum emission, while black contours represent* 0.45, 0.6, 0.8, *and* 0.9 *fractions of the peak line intensity. The synthesized beam is shown in the bottom right corner. A scale bar of* 500 *AU, calculated assuming a distance of* 4.4 *kpc to the source, is shown in the bottom left corner. The coordinate origin is set at the brightest point of the continuum emission, as in Figure 3.1.*

Moment 0 of SO_2 (J_{K_a,K_c} = $21_{2,20}$-$21_{1,21}$) displays a large-scale structure, similar in size to the dust continuum, and has a negative offset in DEC. The structure is shown in Figure 3.11 with black contours being a fraction of 0.45, 0.6, 0.8, 0.9 from the integrated intensity peak. In this case, there are two regions located on the lower zone of the dust contours where the emission is brighter and can be recognized as those enclosed within the 1.62 Jy/Beam · km/s contour. However, the peak intensity of the emission has a value of 1.83 Jy/Beam · km/s located inside the right brighter region at (0.065″,−0.065″). This bright point is offset by 0.091″ from the center of the dust continuum.

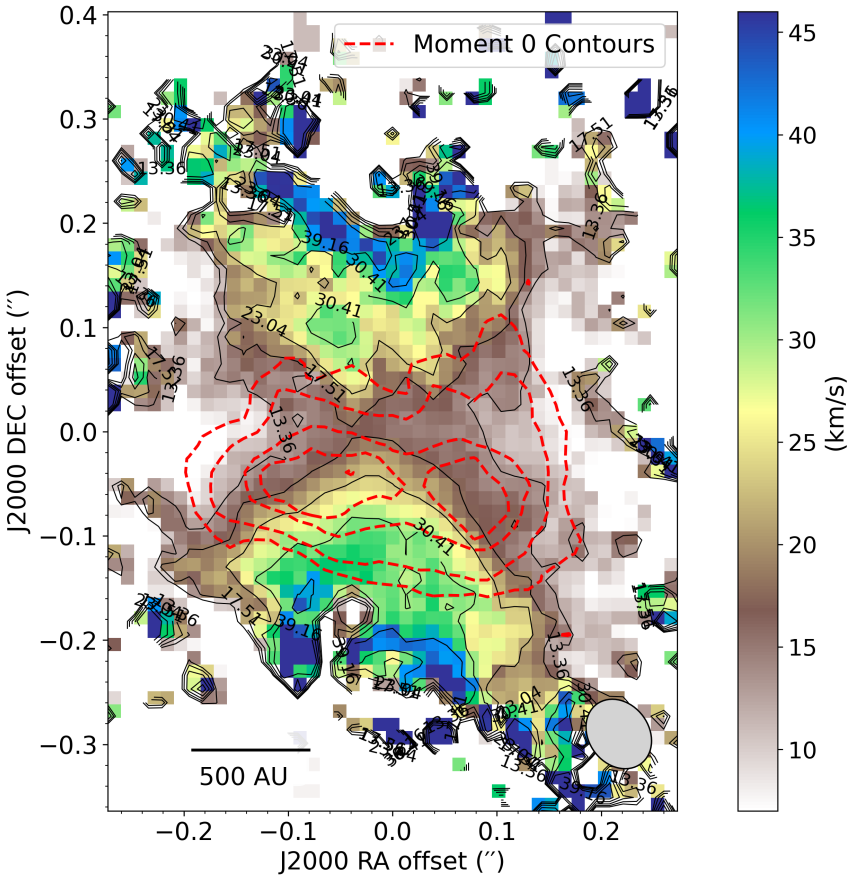

Figure 3.12: *Moment 2 (kinematic distribution map) of the SO_2 (J_{K_a,K_c} = $4_{3,1}$ - $3_{2,2}$) emission. Red contours trace the integrated intensity (Moment 0; see black contours in Fig. 3.5), while black contours represent* 0.29, 0.38, 0.5,0.66, *and* 0.85 *fractions of the maximum velocity. The synthesized beam is shown in the bottom right corner. A scale bar of* 500 *AU, calculated assuming a distance of* 4.4 *kpc to the source, is shown in the bottom left corner. The coordinate origin is set at the brightest point of the continuum emission, as in Figure 3.1.*

Figure 3.12 shows the Moment 2 map computed for the SO_2 (J_{K_a,K_c} = $21_{2,20}$-$21_{1,21}$) line as a bipolar structure. Red contours are the spatial representation of the emission, as in Figure 3.11. Inside the red contours, we define a significant area to study. Moment 2 of SO_2 (J_{K_a,K_c} = $21_{2,20}$-$21_{1,21}$) shows that the velocity range within the two brightest contours covers from 10 km/s to ≈ 30 km/s.

Lines	RA size		DEC size	
	(″)	(AU)	(″)	(AU)
Dust	0.34	1494.71	0.19	837.60
^{13}CO (J = 3 - 2)	0.43	1861.82	0.47	2064.21
SO_2 (J_{K_a,K_c} = $4_{3,1}$ - $3_{2,2}$)	0.42	1839.91	0.36	1577.07
SO_2 (J_{K_a,K_c} = $21_{2,20}$-$21_{1,21}$)	0.34	1401.84	0.22	963.76

Table 3.4: *Estimated Moment 0 sizes for each spectral line, given in (″) and (AU) (assuming a distance of 4.4 kpc to the source).*

Chapter 4

Discussion and Conclusions

4.1 Discussion

The evolutionary paths in the final stages for low and intermediate-mass stars are poorly understood. PNe are complex structures with various morphologies, including spherical, elliptical, multipolar, axisymmetric, or irregular. The cause of this variety of shapes is not well understood. Hydrodynamic models for interacting stellar winds do not predict the structures formed in the early post-AGB phase. Observations are essential for providing models with accurate parameters to understand post-AGB structures better.

IRAS 15445-5449 is a post-AGB star. Generally, these types of sources have conditions that lead formation of molecules. Radio continuum emission was reported before by (Bains et al., 2009) and (Pérez-Sánchez et al., 2013). In this work, we present the highest-resolution continuum observations of the source to date. The dust continuum emission detected with ALMA outlines a large-scale structure that contains the cold dust located near the base of the high-velocity outflow. Its structure is shown in Figure 3.1. Dust is an essential catalyst for the evolution of chemistry in these types of environments. Molecules such as OH, H_2O (Deacon et al., 2004; Sevenster et al., 1997), H_2 (Pérez-Sánchez et al., 2018), ^{12}CO, $C^{18}O$ (Khouri et al., 2021) among others have been detected in the source. With ALMA observations, we identified ^{13}CO (J = 3 - 2) and different transitions of SO_2 presented in Figure 2.2. These molecules, with their specific transitions, were included in catalogs of molecules detected in interstellar and circumstellar clouds (Lovas, 2004), (Lovas, 1985), and in surveys of similar objects as the molecular cloud Orion A (Jewell et al., 1989). What most of them have in common is the presence of oxygen, leading to the conclusion that the CSE of IRAS 15445-5449 is oxygen-rich.

The Hollenbach and McKee (1989) study described the evolution of oxygen chemistry in shocked molecular gas through a set of reactions that occur under appropriate temperature and density conditions in the post-shock gas. It is not a coincidence that the molecules that Hollenbach and McKee (1989) described (H_2, OH, H_2O, and CO) were the same as those found in the observations. Without post-shock conditions, these types of molecules could not be formed. The presence of SO_2 in the CSE of IRAS 15445-5459 suggests the occurrence of shocks at high velocities or J-shocks (Hollenbach and McKee, 1989). The kinematic distribution is presented in Figure 4.1 as the comparison of our three emission lines. The two brightest contours of the spatial

distribution cover ranges of velocities that are higher for ^{13}CO (J = 3 - 2), reaching values of ≈ 50 km/s. SO_2 (J_{K_a,K_c} = $4_{3,1}$ - $3_{2,2}$) reaches maximum values of ≈ 40 km/s and SO_2 (J_{K_a,K_c} = $21_{2,20}$-$21_{1,21}$) reaches ≈ 30 km/s, being the line covering a lower range of velocities than the others. The spatial distribution of SO_2 (J_{K_a,K_c} = $21_{2,20}$-$21_{1,21}$) covers just the southern part of the distribution. According to (Hollenbach et al., 2013), J-shocks in molecular clouds are characterized by velocities exceeding 40 km/s. Consequently, ^{13}CO (J = 3 - 2) and SO_2 (J_{K_a,K_c} = $4_{3,1}$ - $3_{2,2}$) are likely to form under these high-velocity shock conditions. OH and H_2O profiles observed by (Deacon et al., 2007) show velocity ranges of −200 to −100 km/s and −145 to −54 km/s, respectively. The velocity ranges obtained for our ^{13}CO (J = 3 - 2) and SO_2 (J_{K_a,K_c} = $4_{3,1}$ - $3_{2,2}$) transitions (Table 3.3) are larger. This large range of velocities could be explained assuming that in our work, we are seeing regions moving in different directions with respect to the line-of-sight.

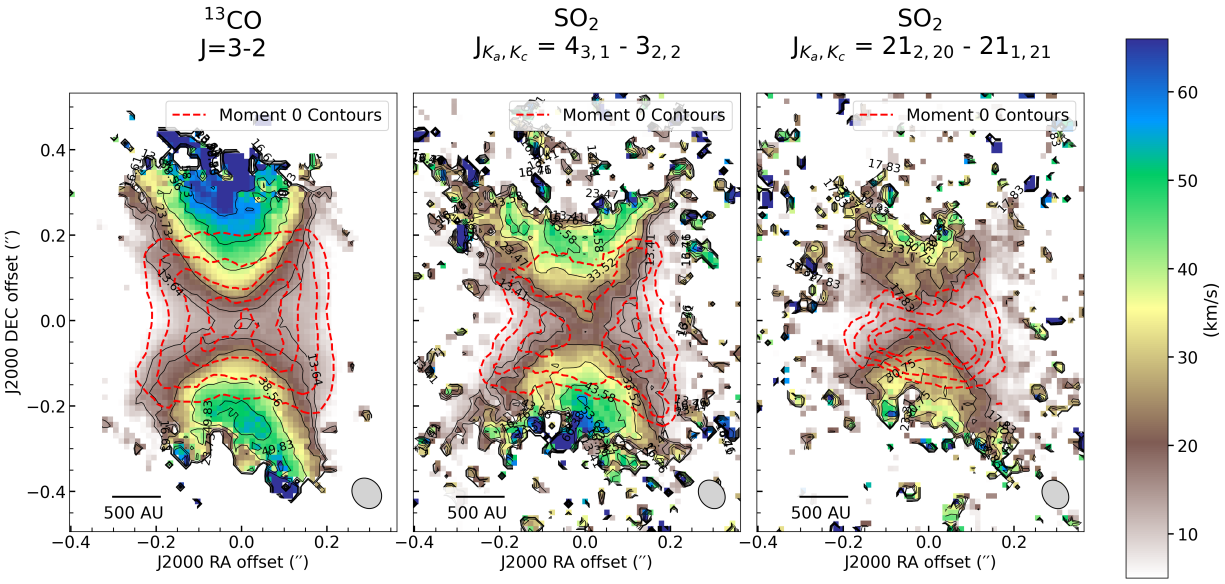

Figure 4.1: *Comparison between moment 2 (kinematic distribution map) for the ^{13}CO (3 - 2), SO_2 ($4_{3,1}$ - $3_{2,2}$), and SO_2 ($21_{2,20}$-$21_{1,21}$) line emission (left to right). Red contours trace the integrated intensity (Moment 0; see black contours in Fig. 3.5, 3.8, and 3.11), while black contours represent fractions of the maximum velocity of each line (See values in Fig. 3.6, 3.9, and 3.12). The synthesized beam is shown in the bottom right corner. A scale bar of 500 AU, calculated assuming a distance of 4.4 kpc to the source, is shown in the bottom left corner. The coordinate origin is set at the brightest point of the continuum emission, as in Figure 3.1.*

From Figure 4.2, we can recognize regions of material over dust contours that are more intense than the rest of the emission. The intensity peaks of the lines are offset by less than 0.12 arcsec from the center of the dust contours. Since dust is essential for the formation of these molecules, it is expected that the gas distribution overlaps with the dust and is concentrated near the center. In addition, we know from (Neufeld and Hollenbach, 1994) that CO, OH, and H_2O are important coolants in the post-shock region, so their presence found in observations implies that the region is cooling down.

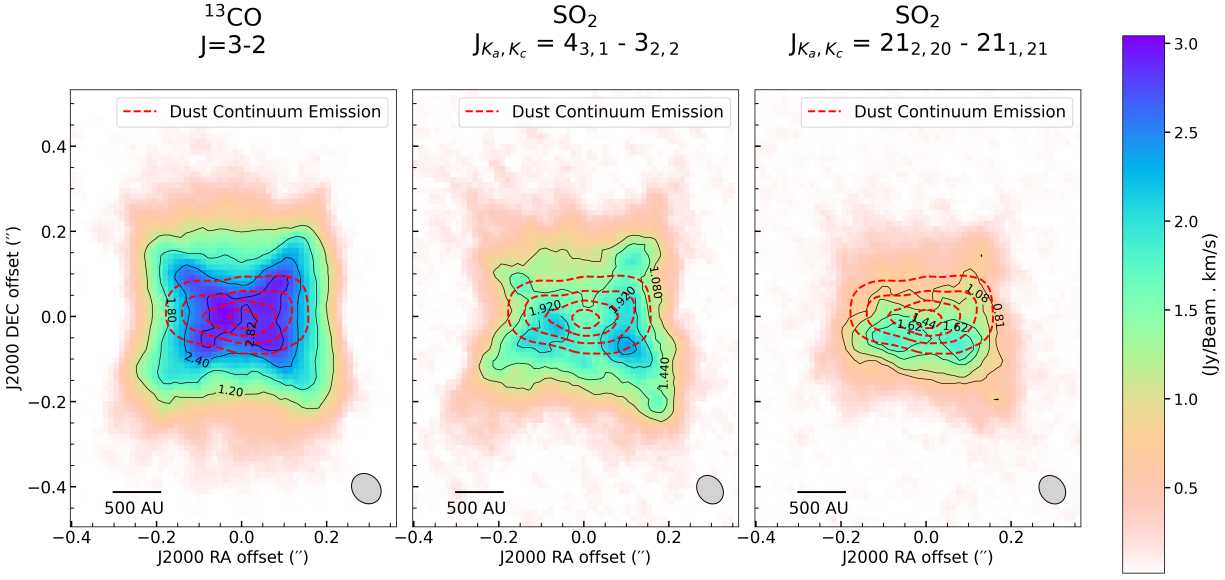

Figure 4.2: *Comparison between moment 0 (integrated intensity map) for the ^{13}CO (3 - 2), SO_2 ($4_{3,1}$ - $3_{2,2}$), and SO_2 ($21_{2,20}$-$21_{1,21}$) line emission (left to right). Red contours trace the dust continuum emission, while black contours represent fractions of the peak line intensity of each line (See values in Fig. 3.5, 3.8, and 3.11). The synthesized beam is shown in the bottom right corner. A scale bar of 500 AU, calculated assuming a distance of 4.4 kpc to the source, is shown in the bottom left corner. The coordinate origin is set at the brightest point of the continuum emission, as in Figure 3.1.*

The RA and DEC PV diagrams (Figure 3.2 and 3.3) give us a first approximation of the structure of the emission. There are some differences between the three line transitions in both diagrams. Emission of SO_2 (J_{K_a,K_c} = $21_{2,20}$-$21_{1,21}$) is lower than the other two lines, but also is smaller. ^{13}CO (J = 3 - 2) is the brightest one and the least distorted. By computing the integrated intensity (Moment 0) and velocity field (Moment 2) maps and comparing them, we found trends similar to those seen in the PV diagrams. The size and intensity comparison of the moment maps for all three spectral lines is shown in Figures 4.2 and 4.1. From the emission lines, the ^{13}CO (J = 3 - 2) line is the brightest and the widest of the three. Carbon monoxide also has better S/N and a more symmetric shape, extending beyond what the continuum traces. Different than the ^{13}CO (J = 3 - 2) and the SO_2 (J_{K_a,K_c} = $4_{3,1}$ - $3_{2,2}$) lines, the spatial distribution of the SO_2 (J_{K_a,K_c} = $21_{2,20}$-$21_{1,21}$) emission overlaps with only part of the continuum emission. PV diagrams show a size scale corresponding to the estimation for a distance of 4.4 kpc. Sizes of all structures are of the order of a few thousand AU for that distance.

Radio observations show that there are sources with high-velocity collimated jets that correspond to AGB and post-AGB stars (Contreras et al., 2018). The origin of the jets is poorly understood. Models try to demonstrate potential magnetic fields or common envelope evolution (Khouri et al., 2021) to explain the physics of the moving material that is shaping the future PN. IRAS 15445-5449 is an extended source with a bipolar morphology, as is shown in Figure 1.5. Moment 2 maps (Figure 4.1) are consistent with IR (Lagadec et al., 2011) observations. A collimated bipolar structure is traced by molecular gas moving at high velocities. This structure shows that the gas dynamics are dominated by expansion motions, rather than rotation. IR observations

by (Lagadec et al., 2011) reveal the structure of the hot gas and the high-velocity outflows. In contrast, the ALMA radio observations presented in this work trace the cold gas regions at the base of the jet. These regions have sizes of < 0.5 arcsec as reported in Table 3.1. When comparing with the scale in Figure 1.5, we can see that the cold gas is located in a small region at the center of the source. This work can help us better understand the morphology of these types of sources in regions close to the central star.

There is some contamination on the ^{13}CO (J = 3 - 2) line between -40 and -50 km/s, both in the PV diagrams (Figure 3.2 and 3.3) as a horizontal missing information and in the mean line emission (Figure 3.4) as an absorption line. IRAS 15445-5449 is located near the galactic plane, and an absorption line product of CO gas in the galaxy could be the reason. Khouri et al. found something similar with their ^{12}CO line and describe it as large-scale Galactic CO contamination.

Systemic velocity of IRAS 15445-5449 has been redefined with time as the resolution of the observations was getting better. First, (Deacon et al., 2007) assumed a $v_{sys} = -150$ km/s due to an irregular OH line profile. With observation performed by SINFONI/VLT, a new systemic velocity was calculated to be the center velocity of a better resolution H_2 line emission profile with a value of -96.4 ± 34 km/s (Pérez-Sánchez et al., 2018). On the other hand, when identifying the spectral lines, we noticed a shift between the line plotted by the CDMS catalog and the center of the spectral line emission. We corrected that using a velocity shift of -90 km/s, and we use it as an approximation of a new definition of the systemic velocity. The ^{13}CO(J = 3 - 2) line is an excellent tracer of the systemic velocity of these sources because the molecule is distributed symmetrically and close to the central star. Consequently, its central velocity is likely to match the systemic velocity of the star. We presented the parameters of fitting emission lines with a two-gaussian model, which can be found in Figure 3.4 for ^{13}CO (J = 3 - 2). From the fitting of that line, we obtained a systemic velocity of $v_{sys} = -85.8$ km/s, which we define as the new systemic velocity of IRAS 15445–5449. This result is confirmed by the velocity ranges in the Figure 3.3 and 3.2. Notice that the center of the structure along the y-axis is offset toward positive values.

The source was classified as a YSO using the information of a ^{13}CO (J = 1 - 0) line emission centered at -44 km/s (Urquhart et al., 2007a). As we discussed before, the center of the ^{13}CO line is a good tracer for the system velocity of the source. Even if ^{13}CO (J = 3 - 2) is a different transition, our results show a significant discrepancy with a systemic velocity of -44 km/s. Contamination reported due to the CO in the galactic plane can be the reason for the confusion, as the absorption CO line is located close to -40 km/s. (Pérez-Sánchez et al., 2013) reported similar results, comparing OH and H_2O observations from (Deacon et al., 2007) with ^{13}CO (1–0) data from (Urquhart et al., 2007a), and concluded that a YSO classification was unlikely.

4.2 Conclusions

The presence of ^{13}CO and SO_2 suggests an oxygen-rich environment with high-velocity shocks. Moment 2 velocity ranges for ^{13}CO (J = 3 - 2) and SO_2 ($J_{K_a,K_c} = 4_{3,1}$ - $3_{2,2}$) exceed 40 km/s, and are consistent with J-shock conditions. SO_2 ($J_{K_a,K_c} = 21_{2,20}$-$21_{1,21}$) shows lower velocities and

a more concentrated spatial distribution. The spatial distribution of molecular emission overlaps the dust contours, showing that dust plays an important role in molecular reformation as reported by Hollenbach and McKee (1989). The overlap between gas and dust and the presence of CO, OH, and H_2O suggest that the region is a post-shock environment with active cooling. PV diagrams and Moment 0 and 2 maps reveal that ^{13}CO (J = 3 - 2) is the brightest and most symmetric line. The systemic velocity of IRAS 15445-5449 is redefined as $v_{sys} = -85.8$ km/s based on the ^{13}CO (J = 3 - 2) line.

Observations indicate a bipolar and collimated morphology, consistent with previous infrared studies, and the gas dynamics are dominated by expansion rather than rotation. ALMA data trace the cold gas at the base of the jet, helping us to better understand, from another perspective, the morphology of these types of sources. Some contamination in the ^{13}CO (J = 3 - 2) line is likely caused by galactic CO absorption along the line of sight. The wide variety of morphologies observed in PNe remains an open problem in astronomy, and the description of a single source cannot provide complete answers. However, the main goal of this work was to describe in great detail the spatial distribution and the velocity field of the molecular emission in this post-AGB star. With the results from our observations and fits, we provide reliable parameters that are key inputs for non-LTE radiative transfer models. A full description of this source can be retrieved by complementing our results with detailed modeling.

Acknowledgements

¿Cómo atrapar una estrella? Es algo que me pregunté incontables veces durante mis primeros años de vida. Crecí amando la astronomía con cada parte de mi ser, buscando de alguna manera la respuesta a esa pregunta. Un día decidí embarcarme en este camino de convertirme en astrónoma y en la Universidad de Antioquia encontré el impulso que necesitaba. A pesar de los altos y bajos, esta carrera me ha enseñado que perseguir los sueños no siempre es sencillo, pero de alguna manera termina valiendo la pena. Sin embargo, yo no llegué hasta aquí sola; de hecho, estoy convencida de que sin las personas que mencionaré a continuación, no estaría aquí escribiendo este pequeño texto.

Quisiera agradecer en primer lugar a mi mamá, Stella. Eres una mujer que me ha dejado incontables enseñanzas en la vida. Me has apoyado incondicionalmente y sé que me amas profundamente, por eso mereces el mayor de los reconocimientos. Gracias por alimentar mi espíritu de científica, por responder a todos los "¿y eso por qué...?" y por darme las herramientas para que pudiera llegar lejos. Voy a agradecer profundamente a mi papá, Carlos. De ti aprendí que el amor no tiene límites y que en los momentos más difíciles siempre hay que seguir adelante.

Una de las personas a las que más necesito agradecer haber llegado hasta aquí es mi abuelita Rosario, que me acogió en su casa durante toda la carrera. Gracias por todo el amor, el apoyo en los momentos difíciles, la compañía, por siempre preocuparte por mí y por todos y cada uno de los almuerzos que llevé a la universidad. La gratitud debe extenderse mucho más allá: gracias a mis tías Ana, Nury y Damaris, a mis primas y primos y a mis hermanos, Juan y Sebas. Gracias por todo su apoyo, porque todos, de alguna manera, pusieron un granito de arena para que yo pudiera llegar donde estoy. Debo agradecer especialmente a mi prima Valentina. Ella, que es mi hermana de otra madre, fue mi compañía y mi apoyo en la vida universitaria.

El agradecimiento hacia mis asesores de tesis es inmenso. Para el profe Esteban, gracias por ser mi mentor durante la carrera. Desde mi pasantía como joven investigadora, Antioquia mira su cielo me enseñó que en Colombia tenemos el material y la fuerza para hacer cosas grandes, de talla internacional, y pienso trabajar para que ese potencial no sea desperdiciado. Tú siempre has buscado que tus estudiantes lleguen tan lejos como puedan, y esta tesis es el reflejo de eso. Para Andrés: tú eres el astrónomo más teso que he conocido en mi vida. Este trabajo no sería ni la mitad de bueno sin toda la ayuda que me brindaste. Gracias por cada consejo, por toda la paciencia y por enseñarme tantas cosas, de la academia y de la vida. Agradezco también a mis profesores del pregrado, especialmente a Juan Carlos Muñoz, Pablo Cuartas, Germán Chaparro y Lauren Flor. No solo por todo lo que aprendí de ustedes, sino por cada vez que me dieron un consejo, me impulsaron a ser mejor o me alegraron el día. Tener profesores con tanta dedicación

por la enseñanza no tiene precio.

Los agradecimientos no estarían completos si no menciono a mis compañeros de camino científico: las personas que compartieron aula de clase conmigo y los que se convirtieron en mis mejores amigos. Agradezco a los Astrococos: Aleja, Alejo, Melkyn, Diego, Samu, Manu y Harold. No podría haber pedido un mejor grupo de amigos con quienes atravesar esta carrera. Su apoyo fue el que me mantuvo de pie en los momentos más difíciles: todas las veces que trasnochamos juntos, todos los trabajos y parciales que enfrentamos uno al lado del otro, pero también todos los parches, las celebraciones y los helados. Yo no habría llegado hasta aquí sin ustedes. De la misma manera, tengo que agradecer a mis compañeros de LUCA, Santi y Jhossua. Junto a ustedes atravesé todas las etapas de esta tesis: desde las primeras reuniones en las que no entendía muy bien lo que estaba haciendo hasta los resultados y la escritura del texto. Ustedes supieron qué decir en cada momento y cómo impulsarme a seguir adelante. Finalmente, agradezco a todos los integrantes del grupo Hermes, Mensajeros de la Ciencia, por encender la chispa de la divulgación científica en mi vida. Las experiencias que he vivido junto a todos ustedes me las llevaré por siempre en el corazón y, desde donde sea que la vida me ponga, seguiré alimentando esa necesidad de invitar a las personas a mirar hacia arriba, hacia las estrellas.

Hay muchas personas a las que no he mencionado y que hicieron parte de este proceso. Estoy agradecida con la vida por poner en mi camino a tantas personas tan increíbles. Para ustedes, solo tengo gratitud y amor. Finalmente puedo decir qué, al terminar mi carrera,

¡Ya tengo una mejor idea de cómo atrapar una estrella!

Medellín, 2025

Marcela Echeverri Gallego

Bibliography

Alm, M., Angerd, G., Lundberg, T., Wölfinger, A., and Oleszko, S. (2019). Circumstellar envelopes of stars on the asymptotic giant branch: The determination of gas mass-loss rates, identification of molecules and detection of dust.

Arp, H. C., Baum, W. A., and Sandage, A. R. (1953). The color-magnitude diagram of the globular cluster m 92. *Astronomical Journal, Vol. 58, p. 4 (1953)*, 58:4.

Bains, I., Cohen, M., Chapman, J. M., Deacon, R. M., and Redman, M. P. (2009). Revealing the transition from post-AGB stars to planetary nebulae: non-thermal and thermal radio continuum observations. , 397(3):1386–1401.

Carroll, B. W. and Ostlie, D. A. (2017). *An introduction to modern astrophysics*. Cambridge University Press.

Caswell, J. L. (1998). Positions of hydroxyl masers at 1665 and 1667 MHz. , 297(1):215–235.

Cohen, M., Chapman, J. M., Deacon, R. M., Sault, R. J., Parker, Q. A., and Green, A. J. (2006). Radio observations of the planetary nebula around the OH/IR star OH354.88-0.54 (V1018 Sco). , 369(1):189–196.

Contreras, C. S., Alcolea, J., Bujarrabal, V., Castro-Carrizo, A., Prieto, L. V., Santander-García, M., Quintana-Lacaci, G., and Cernicharo, J. (2018). Through the magnifying glass: Alma acute viewing of the intricate nebular architecture of oh 231.8+ 4.2. *Astronomy & Astrophysics*, 618:A164.

Deacon, R. M., Chapman, J. M., and Green, A. J. (2004). OH Maser Observations of Likely Planetary Nebulae Precursors. , 155(2):595–622.

Deacon, R. M., Chapman, J. M., Green, A. J., and Sevenster, M. N. (2007). H_2O Maser Observations of Candidate Post-AGB Stars and Discovery of Three High-Velocity Water Sources. , 658(2):1096–1113.

Dirac, P. A. M. (1927). The quantum theory of the emission and absorption of radiation. *Proceedings of the Royal Society of London. Series A, Containing Papers of a Mathematical and Physical Character*, 114(767):243–265.

Draine, B. T. and McKee, C. F. (1993). Theory of interstellar shocks. *In: Annual review of astronomy and astrophysics. Vol. 31 (A94-12726 02-90), p. 373-432.*, 31:373–432.

Einstein, A. (1916). Strahlungs-Emission und Absorption nach der Quantentheorie. *Deutsche Physikalische Gesellschaft*, 18:318–323.

Flower, D. R. and Pineau Des Forêts, G. (2010). Excitation and emission of H2, CO and H2O molecules in interstellar shock waves. , 406(3):1745–1758.

Guillet, V., Jones, A. P., and Pineau Des Forêts, G. (2009). Shocks in dense clouds. II. Dust destruction and SiO formation in J shocks. , 497(1):145–153.

Habing, H. J. and Olofsson, H. (2013). *Asymptotic giant branch stars*. Springer Science & Business Media.

Hartigan, P., Raymond, J., and Hartmann, L. (1987). Radiative bow shock models of herbig-haro objects. *Astrophysical Journal, Part 1 (ISSN 0004-637X), vol. 316, May 1, 1987, p. 323-348.*, 316:323–348.

Herwig, F. (2005). Evolution of asymptotic giant branch stars. *Annu. Rev. Astron. Astrophys.*, 43(1):435–479.

Hewish, A., Bell, S. J., Pilkington, J. D., Frederick Scott, P., and Collins, R. A. (1979). Observation of a rapidly pulsating radio source. In *A Source Book in Astronomy and Astrophysics, 1900–1975*, pages 498–504. Harvard University Press.

Hollenbach, D., Elitzur, M., and McKee, C. F. (2013). Interstellar h2o masers from j shocks. *The Astrophysical Journal*, 773(1):70.

Hollenbach, D. and McKee, C. F. (1989). Molecule formation and infrared emission in fast interstellar shocks. iii-results for j shocks in molecular clouds. *Astrophysical Journal, Part 1 (ISSN 0004-637X), vol. 342, July 1, 1989, p. 306-336.*, 342:306–336.

Jewell, P., Hollis, J., Lovas, F., and Snyder, L. (1989). Millimeter-and submillimeter-wave surveys of orion a emission lines in the ranges 200.7-202.3, 203.7-205.3, and 330-360 ghz. *Astrophysical Journal Supplement Series (ISSN 0067-0049), vol. 70, Aug. 1989, p. 833-864. Research supported by NASA.*, 70:833–864.

Khouri, T., Vlemmings, W. H. T., Tafoya, D., Pérez-Sánchez, A. F., Sánchez Contreras, C., Gómez, J. F., Imai, H., and Sahai, R. (2021). Observational identification of a sample of likely recent common-envelope events. *Nature Astronomy*, 6:275–286.

Lagadec, E., Verhoelst, T., Mékarnia, D., Suáeez, O., Zijlstra, A. A., Bendjoya, P., Szczerba, R., Chesneau, O., van Winckel, H., Barlow, M. J., Matsuura, M., Bowey, J. E., Lorenz-Martins, S., and Gledhill, T. (2011). A mid-infrared imaging catalogue of post-asymptotic giant branch stars. , 417(1):32–92.

Lovas, F. (1985). Microwave spectra of molecules of astrophysical interest. xxii. sulfur dioxide (so2). *Journal of physical and chemical reference data*, 14(2):395–488.

Lovas, F. J. (2004). Nist recommended rest frequencies for observed interstellar molecular microwave transitions—2002 revision. *Journal of Physical and Chemical Reference Data*, 33(1):177–355.

Marr, J. M., Snell, R. L., and Kurtz, S. E. (2015). *Fundamentals of radio astronomy: observational methods*. CRC Press.

Müller, H. S., Thorwirth, S., Roth, D., and Winnewisser, G. (2001). The cologne database for molecular spectroscopy, cdms. *Astronomy & Astrophysics*, 370(3):L49–L52.

Neufeld, D. A. (1987). *Shocked Interstellar Gas in Dense Molecular Clouds.* PhD thesis, Harvard University, Massachusetts.

Neufeld, D. A. and Hollenbach, D. J. (1994). Dense molecular shocks and accretion onto protostellar disks. *Astrophysical Journal, Part 1 (ISSN 0004-637X), vol. 428, no. 1, p. 170-185*, 428:170–185.

Pérez-Sánchez, A., Vlemmings, W., Tafoya, D., and Chapman, J. (2013). A synchrotron jet from a post-asymptotic giant branch star. *Monthly Notices of the Royal Astronomical Society: Letters*, 436(1):L79–L83.

Pérez Sánchez, A. F. (2014). *Molecular line emission in asymmetric envelopes of evolved stars.* PhD thesis, Universitäts-und Landesbibliothek Bonn.

Pérez-Sánchez, A. F., López, R. G., Vlemmings, W., and Tafoya, D. (2018). A detailed study toward the Water fountain IRAS 15445-5449. In Tarchi, A., Reid, M. J., and Castangia, P., editors, *Astrophysical Masers: Unlocking the Mysteries of the Universe*, volume 336 of *IAU Symposium*, pages 355–358.

Pérez-Sánchez, A. F., Vlemmings, W. H. T., and Chapman, J. M. (2011). Water maser polarization of the water fountains IRAS 15445-5449 and IRAS 18043-2116. , 418(2):1402–1407.

Rybicki, G. B. and Lightman, A. P. (2004). *Radiative processes in astrophysics.* John Wiley & Sons.

Ryle, M. (1952). A new radio interferometer and its application to the observation of weak radio stars. *Proceedings of the Royal Society of London. Series A. Mathematical and Physical Sciences*, 211(1106):351–375.

Sevenster, M. N., Chapman, J. M., Habing, H. J., Killeen, N. E. B., and Lindqvist, M. (1997). The ATCA/VLA OH 1612 MHz survey. II. Observations of the galactic Disk region. , 124:509–515.

Thompson, A. R., Moran, J. M., and Swenson, G. W. (2017). *Interferometry and synthesis in radio astronomy.* Springer Nature.

Urquhart, J. S., Busfield, A. L., Hoare, M. G., Lumsden, S. L., Oudmaijer, R. D., Moore, T. J. T., Gibb, A. G., Purcell, C. R., Burton, M. G., and Marechal, L. J. L. (2007a). The RMS survey. ^{13}CO observations of candidate massive YSOs in the southern Galactic plane. , 474(3):891–901.

Urquhart, J. S., Busfield, A. L., Hoare, M. G., Lumsden, S. L., Oudmaijer, R. D., Moore, T. J. T., Gibb, A. G., Purcell, C. R., Burton, M. G., and Marechal, L. J. L. (2007b). VizieR Online Data Catalog: RMS 13CO obs. of YSOs in South Galactic plane (Urquhart+, 2007). VizieR On-line Data Catalog: J/A+A/474/891. Originally published in: 2007A&A...474..891U.

Vickers, S. B., Frew, D. J., Parker, Q. A., and Bojičić, I. S. (2015). New light on Galactic post-asymptotic giant branch stars - I. First distance catalogue. , 447(2):1673–1691.

Abbreviations

AGB	Asymptotic Giant Branch
ALMA	Atacama Large Millimeter/submillimeter Array
ATCA	Australia Telescope Compact Array
AU	Astronomical Unit
CASA	Common Astronomy Software Applications
CDMS	Cologne Database for Molecular Spectroscopy
DEC	Declination
EHT	Event Horizon Telescope
FOV	Field of View
FWHM	Full Width at Half Maximum
HR	Hertzsprung-Russell
IR	Infrared
IRAS	Infrared Astronomical Satellite
LTE	Local Thermodynamic Equilibrium
MSX	Midcourse Space Experiment
PA	Position Angle
PN	Planetary Nebula
PNe	Planetary Nebulae
PV	Position–Velocity
RA	Right Ascension
RG	Red Giant
RGB	Red Giant Branch
RMS	Root Mean Square
SED	Spectral Energy Distribution
SPW	Spectral Window
VLA	Very Large Array
VLBA	Very Long Baseline Array
VLBI	Very Long Baseline Interferometry
VLT	Very Large Telescope
WD	White Dwarf
WF	Water Fountain
YSO	Young Stellar Object
ZAHB	Zero-Age Horizontal Branch